

# The WAGGS project – I. The WiFeS Atlas of Galactic Globular cluster Spectra

Christopher Usher,<sup>1,2\*</sup> Nicola Pastorello,<sup>2,3</sup> Sabine Bellstedt,<sup>2</sup> Adebusola Alabi,<sup>2</sup> Pierluigi Cerulo,<sup>2,4</sup> Leonie Chevalier,<sup>2</sup> Amelia Fraser-McKelvie,<sup>5,6</sup> Samantha Penny,<sup>7</sup> Caroline Foster,<sup>8</sup> Richard M. McDermid,<sup>8,9</sup> Ricardo P. Schiavon<sup>1</sup> and Alexa Villaume<sup>10</sup>

<sup>1</sup>*Astrophysics Research Institute, Liverpool John Moores University, 146 Brownlow Hill, Liverpool L3 5RF, UK*

<sup>2</sup>*Centre for Astrophysics and Supercomputing, Swinburne University of Technology, Hawthorn, VIC 3122, Australia*

<sup>3</sup>*Deakin Software and Technology Innovation Laboratory, Deakin University, Burwood, VIC 3125, Australia*

<sup>4</sup>*Departamento de Astronomia, Universidad de Concepcion, Casilla 160-C, Chile*

<sup>5</sup>*School of Physics and Astronomy, Monash University, Clayton, VIC 3800, Australia*

<sup>6</sup>*Monash Centre for Astrophysics (MoCA), Monash University, Clayton, VIC 3800, Australia*

<sup>7</sup>*Institute of Cosmology and Gravitation, University of Portsmouth, Dennis Sciama Building, Burnaby Road, Portsmouth PO1 3FX, UK*

<sup>8</sup>*Australian Astronomical Observatory, PO Box 915, North Ryde, NSW 1670, Australia*

<sup>9</sup>*Department of Physics and Astronomy, Macquarie University, North Ryde, NSW 2109, Australia*

<sup>10</sup>*University of California Observatories, 1156 High Street, Santa Cruz, CA 95064, USA*

Accepted 2017 March 20. Received 2017 March 20; in original form 2016 November 25

## ABSTRACT

We present the WiFeS Atlas of Galactic Globular cluster Spectra, a library of integrated spectra of Milky Way and Local Group globular clusters. We used the WiFeS integral field spectrograph on the Australian National University 2.3 m telescope to observe the central regions of 64 Milky Way globular clusters and 22 globular clusters hosted by the Milky Way's low-mass satellite galaxies. The spectra have wider wavelength coverage (3300–9050 Å) and higher spectral resolution ( $R = 6800$ ) than existing spectral libraries of Milky Way globular clusters. By including Large and Small Magellanic Cloud star clusters, we extend the coverage of parameter space of existing libraries towards young and intermediate ages. While testing stellar population synthesis models and analysis techniques is the main aim of this library, the observations may also further our understanding of the stellar populations of Local Group globular clusters and make possible the direct comparison of extragalactic globular cluster integrated light observations with well-understood globular clusters in the Milky Way. The integrated spectra are publicly available via the project website.

**Key words:** globular clusters: general – galaxies: abundances – Local Group – galaxies: stellar content.

## 1 INTRODUCTION

To measure the age, chemical composition or initial mass function (IMF) of a stellar population from its integrated light requires reliable stellar population synthesis models. Globular clusters (GCs) provide an important laboratory for testing stellar population synthesis models due to their relatively simple stellar populations. Therefore, the task of studying their stellar populations is much simpler than for galaxies, which contain stars with a wide range of ages and metallicities. In the case of Milky Way (MW) GCs,

detailed chemical abundances are available from high-resolution spectroscopy of individual stars (e.g. Carretta et al. 2009) while ages (e.g. Marín-Franch et al. 2009; VandenBerg et al. 2013) and mass functions (e.g. Paust et al. 2010) are available from resolved imaging. By comparing the stellar population parameters derived from the integrated star light with the parameters measured from individual stars, we can test the reliability of stellar population synthesis models.

Additionally, GCs can be used to gain important insights into how galaxies form and evolve. There is a long history of using GCs to study both our own galaxy (e.g. Shapley 1918; Searle & Zinn 1978) and external galaxies (e.g. Hanes 1977; Burstein et al. 1984; Brodie & Huchra 1991; Cohen, Blakeslee & Ryzhov 1998). Due to their

\* E-mail: [c.g.usher@ljmu.ac.uk](mailto:c.g.usher@ljmu.ac.uk)

high surface brightnesses, the integrated light of GCs can be studied spectroscopically at much greater distances than individual stars. For example, Puzia et al. (2005) studied the stellar populations of GCs around NGC 7192 ( $D = 38$  Mpc) and Misgeld et al. (2011) studied the kinematics of GCs in the Hydra I galaxy cluster ( $D = 47$  Mpc). This allows GCs to be used to perform stellar archaeology beyond the Local Group. Integrated light observations of MW GCs can be directly compared with observations of extragalactic GCs in a model independent way. Large data sets of extragalactic GC spectra are now available with the SAGES Legacy Unifying Globulars and GalaxieS (SLUGGS; Brodie et al. 2014; Forbes et al. 2017) survey providing spectra of more than 4000 GCs in 27 galaxies. Other large data sets are available for a few individual galaxies with spectra observed of 922 GCs around M87 (Strader et al. 2011b; Zhu et al. 2014), of more than 693 GCs around NGC 1399 (Schuberth et al. 2010) and of 563 GCs around NGC 5128 (Woodley et al. 2010).

Although they typically do not show spreads in age or iron abundance (e.g. Carretta et al. 2009), GCs show star-to-star abundance variations in elements such as helium, oxygen and sodium (e.g. Gratton, Carretta & Bragaglia 2012). These variations are often explained as GCs consisting of multiple generations of stars, with the later generation(s) forming out of material enriched by the products of hot hydrogen burning. Even though several scenarios for the formation of multiple generations have been proposed (e.g. Decressin et al. 2007; de Mink et al. 2009; D’Ercole et al. 2010; Denissenkov & Hartwick 2014), none are consistent with observations (Bastian & Strader 2014; Bastian & Lardo 2015; Bastian, Cabrera-Ziri & Salaris 2015). Due to the effects of dynamical evolution, the mass functions of GCs today are usually different (e.g. De Marchi, Paresce & Pulone 2007; Paust et al. 2010) than what would be expected from the effects of stellar evolution on a ‘normal’ IMF. While these properties make GCs less than perfect examples of simple stellar populations, reliable comparisons with stellar population synthesis models are still possible if their mass functions and chemical abundance distributions are well measured. Extragalactic GCs are likely similarly affected by multiple populations and dynamical effects, so comparing extragalactic GC observations to those of MW GCs can be preferable to using models (although the mean stellar populations of MW GCs may not be typical of GCs in all galaxies).

Several studies, including Burstein et al. (1984), Zinn & West (1984), Brodie & Hanes (1986), Bica & Alloin (1986), Armandroff & Zinn (1988), Covino, Galletti & Pasinetti (1995), Cohen et al. (1998), Beasley, Hoyle & Sharples (2002), Puzia et al. (2002), Schiavon et al. (2005) and Pipino & Danziger (2011), have obtained integrated low-resolution spectra of MW, Large Magellanic Cloud (LMC) and Small Magellanic Cloud (SMC) GCs with the aim of stellar population analysis. With the exceptions of Armandroff & Zinn (1988,  $R \sim 2000$ ) and Schiavon et al. (2005,  $R \sim 1600$ ), these studies have been at the low ( $R \sim 600$ ) spectral resolution typical of the Lick system (Worthey 1994; Schiavon 2007). In addition, a few (e.g. Colucci et al. 2011; Larsen, Brodie & Strader 2012; Sakari et al. 2013; Colucci, Bernstein & McWilliam 2017; Larsen, Brodie & Strader 2017) studies have obtained integrated high-resolution ( $R \sim 20000$ ) spectra to measure detailed chemical abundances of MW and MW satellite GCs; however, these studies suffer from small sample sizes (<10 GCs each). Most of these studies, except for Schiavon et al. (2005), have only made their spectral index measurements public and not the spectra themselves. Publicly available spectra make possible the comparison of full observed spectral energy distribution with models and enable the testing of novel analysis techniques.

Recently, interest has been growing in using the redder (redwards of  $H\alpha$ ) regions of the optical wavelength range for stellar population studies, many of which have focused on the calcium triplet (CaT) at 8498, 8542 and 8662 Å. First studied as a metallicity indicator in integrated GC spectra by Armandroff & Zinn (1988), the CaT has been used as an age-insensitive method to estimate metallicities of extragalactic GCs (Foster et al. 2010; Usher et al. 2012; Pastorello et al. 2015) and integrated galaxy light (Foster et al. 2009; Pastorello et al. 2014). Intriguingly, the relationship between CaT strength and GC colour has been observed to vary between galaxies (Foster et al. 2011; Usher et al. 2012, 2015) that could be caused by variations in the colour–metallicity relation or by systematics related to the CaT. Additionally, the reliability of the CaT as a metallicity indicator at high metallicity has been challenged (Chung et al. 2016).

The redder part of the optical region is also of interest to studies of the IMF as it contains spectral features, including the CaT and the sodium doublet at 8190 Å, that are sensitive to the ratio of dwarf to giant stars (e.g. Schiavon et al. 1997; Schiavon, Barbay & Bruzual 2000). While multiple studies (e.g. Conroy & van Dokkum 2012; Ferreras et al. 2013) have claimed that the slope of the IMF increases with stellar mass or other galaxy properties, it is unclear if the stellar population synthesis models used correctly account for abundance variations (e.g. Smith et al. 2015).

Unfortunately, there is a lack of high-quality MW GC-integrated spectra covering the red optical wavelengths. The best existing spectral library of MW GCs (Schiavon et al. 2005) only covers the wavelength range from 3360 to 6430 Å, which does not include lines such as the CaT and the 8190 Å sodium doublet that are utilized in IMF studies. Furthermore, the spectral resolution of Schiavon et al. (2005) is low ( $R \sim 1600$ ) compared to those now available for large numbers of extragalactic GCs (e.g.  $R \sim 5000$  for Usher et al. 2012). Higher spectral resolution data make possible the deblending of spectral lines and more detailed chemical abundances to be measured. Higher resolution spectra can always be degraded for comparison with low-resolution spectra; the reverse is not true.

While the GC system of the MW is relatively well studied, it provides only a limited range of ages and chemical compositions. As different galaxies have different evolutionary histories, this will be reflected in variations in their GC properties such as ages, metallicities and abundance patterns. However, the proximity of other Local Group galaxies allows us to extend this parameter space. As would be expected for galaxies spanning a wide range in stellar mass, the Fornax dwarf spheroidal (Fornax), LMC, SMC and the MW all have different age–metallicity and  $[\alpha/\text{Fe}]$ – $[\text{Fe}/\text{H}]$  relationships (e.g. Harris & Zaritsky 2009; de Boer et al. 2012; Piatti & Geisler 2013; Van der Swaelmen et al. 2013; Davies et al. 2015). Both SMC and LMC host massive young- and intermediate-age star clusters that are rare and difficult to study in the MW (e.g. GLIMPSE-CO1; Kobulnicky et al. 2005; Davies et al. 2011).

To provide a library of integrated spectra of the GCs of the MW and its satellite galaxies with wider wavelength coverage and higher spectral resolution, we have turned to integral field spectroscopy to produce WAGGS – the WiFeS Atlas of Galactic Globular cluster Spectra. Using the Wide-Field Spectrograph (WiFeS) on the Australian National University (ANU) 2.3-metre telescope, we have observed 64 GCs in the MW, 3 in the Fornax dSph, 14 in the LMC and 5 in the SMC. Besides providing spatially resolved spectroscopy at higher resolution ( $R \sim 6800$ ) and wider wavelength coverage (3270–9050 Å) than existing spectral libraries, WAGGS includes more GCs (86) and a wider range of ages (20 Myr–13 Gyr).

This paper is the first in a series of papers based on the WAGGS data. In this paper, we describe our sample selection and the properties of our sample in Section 2. In Section 3, we describe our observations and our data reduction methods. Finally, in Section 4, we discuss planned and possible uses of the WAGGS spectra.

Throughout this paper, we will use the term GC to refer to all observed star clusters even though a number of the massive ( $>10^4 M_{\odot}$ ) star clusters observed in the SMC and LMC are significantly younger than classical GCs. We note that the definition of a GC has been debated in the literature (Forbes & Kroupa 2011; Willman & Strader 2012). With the possible exception of the very youngest ( $\sim 20$  Myr) LMC and SMC star clusters, all of our GCs meet the definition of Kruijssen (2015), namely ‘[a] gravitationally bound, stellar cluster that in terms of its position and velocity vectors does not coincide with the presently star-forming component of its host galaxy’. We note that two objects included in our sample, NGC 5139 ( $\omega$  Cen; e.g. Johnson & Pilachowski 2010) and NGC 6715 (M 54; e.g. Carretta et al. 2010), show significant metallicity spreads and are thought to have formed from the centres of accreted dwarf galaxies (e.g. Ibata et al. 1997; Hilker & Richtler 2000). As such they may be more akin to ultra-compact dwarfs (Pfeffer et al. 2014).

## 2 SAMPLE SELECTION AND PROPERTIES

Our aim in selecting GCs for observation was to obtain a representative sample of GCs rather than a complete one. The starting point for our sample is the Advanced Camera for Surveys (ACS) Globular Cluster Treasury Survey (Sarajedini et al. 2007), which provides high-quality, homogeneous *Hubble Space Telescope* (HST) ACS imaging for 65 Galactic GCs. We supplemented these with the six MW halo GCs observed with ACS in a similar manner by Dotter, Sarajedini & Anderson (2011). Many of these clusters also have UV and blue *HST* Wide Field Camera 3 (WFC3) photometry from the *HST* UV Legacy Survey of Galactic Globular Clusters (Piotto et al. 2015). High-quality age measurements (e.g. Marín-Franch et al. 2009; VandenBerg et al. 2013) and horizontal branch morphologies (Milone et al. 2014) are available for the majority of these GCs. We restricted our sample to GCs with declinations lower than  $+30^{\circ}$  so that they would be observable from Siding Spring Observatory and central surface brightness brighter than  $\mu_V \sim 20$  mag arcsec $^{-2}$  so that we could obtain high signal-to-noise ratios (S/N) in reasonable exposure times. We prioritized GCs that already have detailed chemical abundance measurements available for multiple stars such as the GCs observed by Carretta et al. (2009), by ESO-*Gaia* (Gilmore et al. 2012) and by APOGEE (Mészáros et al. 2015; Majewski, APOGEE Team & APOGEE-2 Team 2016). We include NGC 5139 and NGC 6715 to test how well the mean properties of complex stellar populations can be measured from integrated light.

In addition, we observed a number of bright MW GCs, not in the ACS Globular Cluster Treasury Survey, that have published chemical abundances from high-resolution spectroscopy, many of which have *HST* Wide Field and Planetary Camera 2 photometry from Piotto et al. (2002) and relative ages from De Angeli et al. (2005). We also observed a number of bright but relatively poorly studied GCs, including NGC 5824, NGC 6284, NGC 6316, NGC 6333 and NGC 6356, both to improve our coverage of bulge and halo GCs and to provide a larger sample of GCs for integrated light abundance studies.

To expand the range of ages and chemical compositions observed, we supplemented our sample with GCs in MW satellites. We targeted three old (age  $>10$  Gyr) GCs in the Fornax dSph, one in the

SMC and four in the LMC. We also observed eight intermediate age ( $1 < \text{age} < 10$  Gyr) and six young (age  $< 1$  Gyr) GCs in the LMC and SMC. Two of our MW GCs, NGC 5634 and NGC 6715 can be associated with the disrupting Sagittarius dwarf spheroidal galaxy on the basis of their positions and kinematics (e.g. Bellazzini, Ferraro & Ibata 2003; Law & Majewski 2010) while a third (NGC 4147) shows only weak evidence of being associated with the Sagittarius dwarf (Law & Majewski 2010). As with our MW targets, we prioritized bright GCs with the *HST* imaging and high-resolution spectroscopy.

An overview of the properties of the sample GCs is shown in Fig. 1 and given in Table 1. For the MW GCs we use metallicities, distances and structural parameters from the 2010 edition of the Harris (1996) catalogue. The Harris metallicities are on the Carretta et al. (2009) scale but come from a range of sources. For MW GCs, we prefer ages estimated by Dotter et al. (2010, 2011), supplemented by ages estimated by Milone et al. (2014) using the same techniques and models. Together, these are the largest homogeneous samples of MW GC ages. Other sources of ages are given in Table 1. We scaled the De Angeli et al. (2005) and Meissner & Weiss (2006) ages to match the Dotter et al. (2010, 2011) measurements by using GCs of similar ages and metallicities in both studies. Origlia et al. (2008) claim that NGC 6440 has the same age as NGC 104; therefore, we assign NGC 6440 the same age as calculated by Dotter et al. (2010, 12.75 Gyr) for NGC 104.

For Fornax, the LMC and the SMC, we adopted the distances used by McLaughlin & van der Marel (2005): 137, 50 and 60 kpc, respectively. We drew the structural parameters of GCs around these galaxies from several studies listed in Table 1, using the values provided by McLaughlin & van der Marel (2005) when available. Likewise, ages and metallicities for the GCs of MW satellites come from a range of studies listed in Table 1. For the satellite galaxies, we preferred metallicities from high-resolution spectroscopy to those from the resolved star CaT strengths, and CaT-based metallicities to those based on resolved colour–magnitude diagrams. For the LMC and SMC clusters with metallicities based on the strength of the CaT, we recalculated the metallicities using CaT–metallicity relations based on the Carretta et al. (2009) metallicity scale. For NGC 416, NGC 419 and NGC 1846, for which metallicities were derived using equation 5 of Cole et al. (2004) by Glatt et al. (2009) or Grocholski et al. (2006), we recalculated the metallicities using equation 6 of Cole et al. (2004). For NGC 1868, we converted the metallicity of Olszewski et al. (1991) from the Zinn & West (1984) scale to the Carretta et al. (2009) scale using the equation provided by Carretta et al. (2009).

We estimated stellar masses for each of our GCs using their extinction corrected *V*-band absolute magnitudes. For each GC, we used the extinction measurements provided by the same source that provided the structural parameters (the Harris catalogue for MW GCs, McLaughlin & van der Marel 2005 for most others). Stellar population synthesis models (e.g. Conroy, Gunn & White 2009) predict that the *V*-band mass-to-light ratio ( $M/L_V$ ) increases with metallicity, while dynamical studies (e.g. Strader, Caldwell & Seth 2011a; Baumgardt 2017) show that the  $M/L_V$  decreases with metallicity or remains constant. For this reason, we have adopted the agnostic approach of a constant  $M/L_V = 2$  for all GCs older than 10 Gyr. For younger GCs, we follow McLaughlin & van der Marel (2005) and use the Bruzual & Charlot (2003) derived values. We use luminosity-based masses as dynamical masses are not available for all GCs in our sample. The properties shown in Fig. 1 and given in Table 1 highlight the range of sample properties but may not be the final values adopted for future analysis.

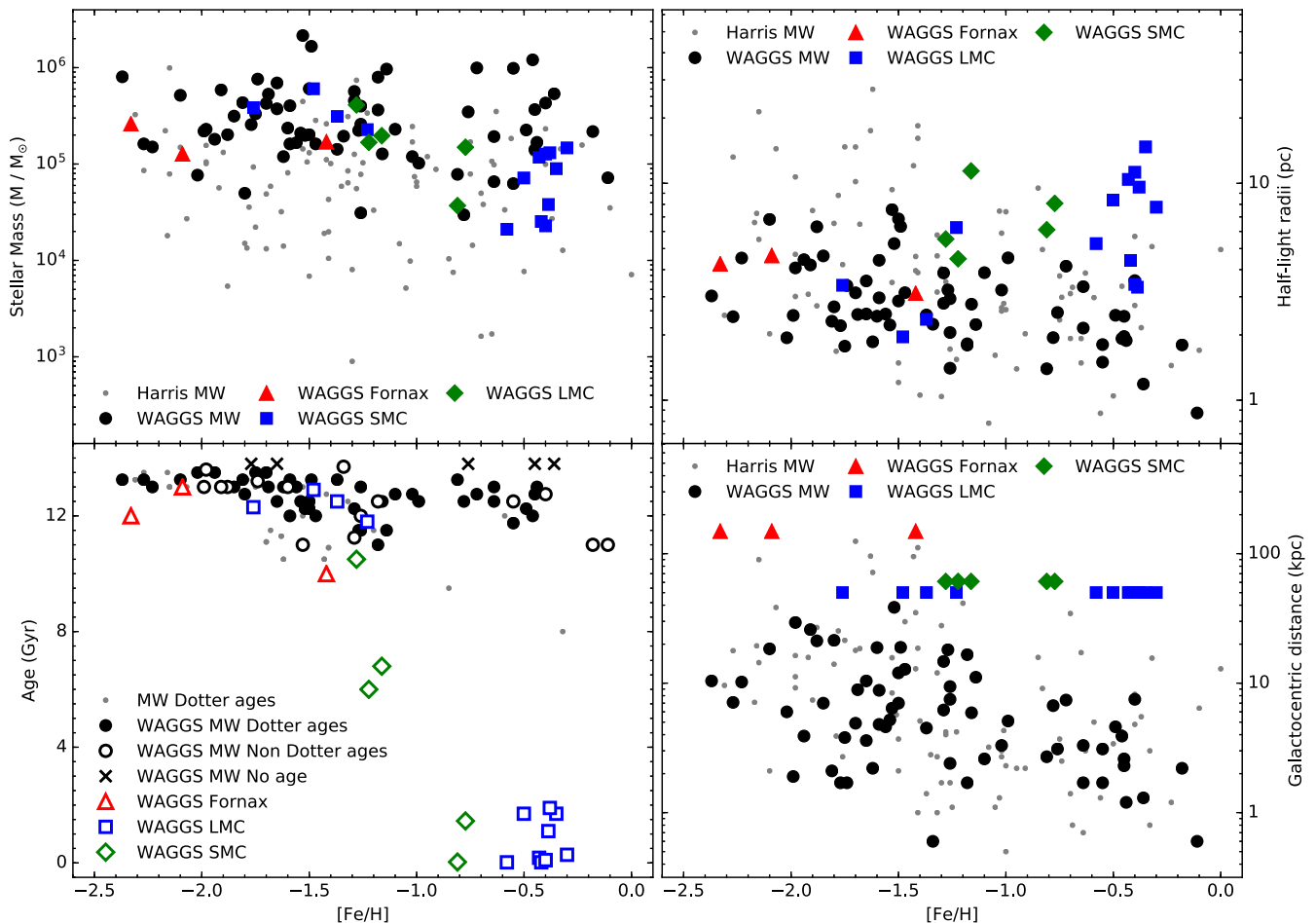


**Figure 1.** General properties of the WAGGS sample. Top left: stellar mass from V-band luminosity versus metallicity. WAGGS GCs in the MW are plotted as black circles, WAGGS GCs in Fornax as red triangles, WAGGS GCs in the LMC as blue squares and WAGGS GCs in the SMC as green diamonds. Grey points are MW GCs from the 2010 edition of the Harris (1996) catalogue. The WAGGS sample is biased towards higher masses relative to the MW population. Bottom left: age versus metallicity. The filled WAGGS points have ages from Dotter et al. (2010), Dotter et al. (2011) or Milone et al. (2014); open points have ages from other sources. MW GCs marked with crosses have no published ages and have been assigned ages of 13.8 Gyr for the purposes of illustration. The grey points are other MW GCs with ages from Dotter et al. (2010), Dotter et al. (2011) or Milone et al. (2014). The WAGGS sample covers much of the MW GCs age–metallicity space as well as the range of GC ages in the LMC and SMC. Top right: half-light radius versus metallicity. The WAGGS GCs are plotted as in the top left panel and the grey points are all MW GCs in the Harris catalogue. Bottom right: galactocentric distance versus metallicity. The WAGGS GCs and the Harris MW GCs are plotted as in the top right panel. The WAGGS sample misses faint, extended GCs found in the MW halo as well as heavily extinguished GCs in the bulge.

In general, we favoured GCs with higher central surface brightnesses in order to maximize the number of GCs observed in the available observing time. As such, our sample suffers from a few biases. First, our sample is biased towards more massive GCs (see the upper left panel of Fig. 1). We note that extragalactic GC studies are usually limited to the mean of the GC luminosity function, if not brighter. Massive GCs would also be better for stellar population comparisons as the effects of stochastic sampling of the IMF would be less severe. Secondly, our sample is biased towards spatially concentrated GCs (see the upper right panel of Fig. 1). As such, we miss many of the faint, extended GCs in the MW halo. Thirdly, our sample is biased against GCs with high foreground reddening. While this biases our sample against bulge GCs, these highly reddened GCs are typically poorly studied, thus making them poor choices for testing stellar population synthesis models. These selection biases are mostly shared with previous integrated light studies. Our sample includes 35 of the 40 GCs observed by Schiavon et al. (2005) and 10 of the 12 GC observed by Puzia et al. (2002). Com-

pared to Schiavon et al. (2005) and Puzia et al. (2002), our sample extends to lower mass MW GCs and includes more metal-poor GCs and halo GCs.

Since we only observed a single, central pointing for each GC and the GCs in our sample span a wide range of heliocentric distances (from 2.2 kpc for NGC 6121 to 137 kpc for the Fornax GCs), the fraction of GC light we observed varies dramatically. This is illustrated in Fig. 2, where we show both the nearest (NGC 6121) and farthest (Fornax 3) GCs in sample as well a GC at the median distance (10 kpc, NGC 2808). The fraction of GC V-band light within the WiFeS field of view was estimated from surface brightness profiles calculated from the structural parameters given in Table 1 using the LIMEPY code (Gieles & Zocchi 2015) and a King (1966) profile. The fraction of observed luminosity ranges from 0.005 (NGC 5139) to 0.81 (Fornax 4) with a median of 0.17 (0.12 for MW GCs). These observed light fractions are shown in the top panel of Fig. 3. In the bottom panel of Fig. 3, we also show the ratios of the core radius and half-light radius to the equivalent

**Table 1.** General properties of the WAGGS sample.

ID	Name	Galaxy	RA	Dec	$d_{gc}$	[Fe/H]	Age	$R_c$	$R_h$	$\mu_{V0}$	$A_V$	GC Mass	FoV Mass	[Fe/H]	Age	Structural	
(1)	(2)	(3)	(4)	(5)	(6)	(7)	(8)	(9)	(10)	(11)	(12)	(13)	(14)	(15)	(16)	(17)	(18)
			[°]	[°]	[kpc]	[dex]	[Gyr]	[arcsec]	[arcsec]	[mag arcsec <sup>-2</sup> ]	[mag]	[log M <sub>⊙</sub> ]	[log M <sub>⊙</sub> ]	source	source	source	
NGC 104	47 Tuc	MW	6.024	-72.081	4.5	7.4	-0.72	12.8	22	14.4	0.12	6.0	4.7	H	Do10	H	
NGC 121		SMC	6.701	-71.536	60.0	61.0	-1.28	10.5	10	18.3	0.45	5.6	5.2	Da16	GI08a	McL05	
NGC 330		SMC	14.074	-72.463	60.0	61.0	-0.81	0.03	8	16.5	0.20	4.6	4.2	Hf99	Si02	McL05	
NGC 361		SMC	15.542	-71.605	60.0	61.0	-1.16	6.8	24	20.2	0.21	5.3	4.5	Da98	Mi98	McL05	
NGC 362		MW	15.809	-70.849	8.6	9.4	-1.26	11.5	11	14.8	0.15	5.6	4.9	H	Do10	H	
NGC 416		SMC	16.994	-72.355	60.0	61.0	-1.22	6.0	10	18.5	0.39	5.2	4.9	GI09	GI08b	McL05	
NGC 419		SMC	17.072	-72.883	60.0	61.0	-0.77	1.4	13	17.8	0.31	5.2	4.9	GI09	Gol4	GI09	
Fornax 3	NGC 1049	Fornax	39.951	-34.258	137.0	149.0	-2.33	12.0	2	17.1	0.11	5.4	5.3	La12	deB16	McL05	
Fornax 4		Fornax	40.032	-34.536	137.0	149.0	-1.42	10.0	2	17.5	0.43	5.2	5.1	La12	deB16	McL05	
Fornax 5		Fornax	40.588	-34.102	137.0	149.0	-2.09	13.0	1	17.6	0.10	5.1	5.0	La12	deB16	McL05	
NGC 1261		MW	48.068	-55.216	16.3	18.1	-1.27	11.5	21	17.7	0.03	5.3	4.4	H	Do10	H	
NGC 1786		LMC	74.783	-67.745	50.1	50.0	-1.76	12.3	4	16.4	0.39	5.6	5.3	Mu10	Ge97	McL05	
NGC 1783		LMC	74.787	-65.987	50.1	50.0	-0.35	1.7	38	20.4	0.02	5.0	3.9	Mu08	Gol4	Go06+11	
NGC 1846		LMC	76.891	-67.461	50.1	50.0	-0.50	1.7	26	19.6	0.08	4.9	4.1	Gr06	Gol4	Go06+09	
NGC 1850		LMC	77.186	-68.762	50.1	50.0	-0.40	0.1	11	16.7	0.32	5.1	4.4	Ni15	Ni15	McL05	
NGC 1856		LMC	77.372	-69.128	50.1	50.0	-0.30	0.3	7	16.8	0.71	5.2	4.6	Bal13	Bal13	McL05	
NGC 1866		LMC	78.413	-65.466	50.1	50.0	-0.43	0.2	11	17.3	0.40	5.1	4.4	Mu11	Bal13	McL05	
NGC 1851		MW	78.528	-40.047	12.1	16.6	-1.18	11.0	5	14.2	0.06	5.6	5.0	H	Mi14	H	
NGC 1868		LMC	78.651	-63.955	50.1	50.0	-0.39	1.1	6	17.8	0.41	4.6	4.3	O191	Ke07	McL05	
NGC 1898		LMC	79.177	-69.656	50.1	50.0	-1.23	11.8	9	18.6	0.26	5.4	4.9	Jo06	O198	McL05	
NGC 1916		LMC	79.652	-69.407	50.1	50.0	-1.48	12.9	3	15.3	0.58	5.8	5.6	Co11	Ma03	McL05	
NGC 1904	M 79	MW	81.046	-24.525	12.9	18.8	-1.60	13.0	10	16.0	0.03	5.4	4.6	H	DeA05	H	
NGC 1978		LMC	82.188	-66.236	50.1	50.0	-0.38	1.9	18	18.4	0.21	5.1	4.6	Mu08	Mu07	Fi92+Go06	
NGC 2004		LMC	82.678	-67.286	50.1	50.0	-0.58	0.02	6	16.2	0.36	4.3	3.9	Ni15	Ni15	McL05	
NGC 2019		LMC	82.986	-70.160	50.1	50.0	-1.37	12.5	2	15.8	0.43	5.5	5.3	Jo06	O198	McL05	
NGC 2100		LMC	85.538	-69.212	50.1	50.0	-0.42	0.02	4	15.6	0.65	4.4	4.1	Pa16	Ni15	McL05	
NGC 2136		LMC	88.241	-69.493	50.1	50.0	-0.40	0.1	7	17.1	0.59	4.4	4.1	Mu12	Ni15	McL05	
NGC 2808		MW	138.013	-64.864	9.6	11.1	-1.14	11.5	15	15.1	0.67	6.0	5.2	H	Mi14	H	
NGC 3201		MW	154.403	-46.412	4.9	8.8	-1.59	12.0	78	19.0	0.73	5.2	3.3	H	Do10	H	
NGC 4147		MW	182.526	18.543	19.3	21.4	-1.80	12.8	5	17.4	0.06	4.7	4.2	H	Do10	H	
NGC 4590	M 68	MW	189.867	-26.744	10.3	10.2	-2.23	13.0	35	18.8	0.15	5.2	3.7	H	Do10	H	
NGC 4833		MW	194.891	-70.876	6.6	7.0	-1.85	13.0	60	18.5	0.98	5.5	3.8	H	Do10	H	
NGC 5024	M 53	MW	198.230	18.168	17.9	18.4	-2.10	13.2	21	17.4	0.06	5.7	4.7	H	Do10	H	
NGC 5139	$\omega$ Cen	MW	201.697	-47.480	5.2	6.4	-1.53	11.0	142	16.8	0.37	6.3	4.1	H	Vi07	H	
NGC 5272	M 3	MW	205.548	28.377	10.2	12.0	-1.50	12.5	22	16.6	0.03	5.8	4.5	H	Do10	H	
NGC 5286		MW	206.612	-51.374	11.7	8.9	-1.69	13.0	17	16.2	0.73	5.7	5.0	H	Do10	H	
NGC 5634		MW	217.405	-5.976	25.2	21.2	-1.88	13.0	5	17.2	0.15	5.3	4.5	H	Me05	H	
NGC 5694		MW	219.901	-26.539	35.0	29.4	-1.98	13.6	4	16.5	0.27	5.4	4.9	H	DeA05	H	
NGC 5824		MW	225.994	-33.068	32.1	25.9	-1.91	13.0	4	15.2	0.40	5.8	5.4	H	DeA05	H	
NGC 5904	M 5	MW	229.638	2.081	7.5	6.2	-1.29	12.2	26	16.1	0.09	5.8	4.5	H	Do10	H	
NGC 5927		MW	232.003	-50.673	7.7	4.6	-0.49	12.2	25	16.9	1.37	5.4	4.7	H	Do10	H	
NGC 5986		MW	236.512	-37.786	10.4	4.8	-1.59	13.2	28	17.7	0.86	5.6	4.4	H	Do10	H	

Table 1 – continued

ID	Name	Galaxy	RA	Dec	$d_{\odot}$	$d_{gc}$	[Fe/H]	Age	$R_c$	$R_l$	$\mu_{450}$	$A_V$	GC mass	FoV mass	[Fe/H]	Age	Structural
(1)	(2)	(3)	(4)	(5)	(6)	(7)	(8)	(9)	(10)	(11)	(12)	(13)	(14)	(15)	(16)	(17)	(18)
NGC 6093	M 80	MW	244.260	-22.976	10.0	3.8	-1.75	13.5	9	37	15.1	0.55	5.5	5.0	H	Do10	H
NGC 6121	M 4	MW	245.897	-26.526	2.2	5.9	-1.16	12.5	70	260	18.0	1.07	5.1	3.1	H	Do10	H
NGC 6139		MW	246.918	-38.849	10.1	3.6	-1.65	-	9	51	17.2	2.29	5.6	4.8	H	-	H
NGC 6171	M 107	MW	248.133	-13.054	6.4	3.3	-1.02	12.8	34	104	18.9	1.01	5.1	3.6	H	Do10	H
NGC 6218	M 12	MW	251.809	-1.949	4.8	4.5	-1.37	13.2	47	106	18.1	0.58	5.2	3.5	H	Do10	H
NGC 6254	M 10	MW	254.288	-4.100	4.4	4.6	-1.56	13.0	46	117	17.7	0.86	5.2	3.7	H	Do10	H
NGC 6266	M 62	MW	255.303	-30.114	6.8	1.7	-1.18	12.5	13	55	15.1	1.44	5.9	5.1	H	DeA05	H
NGC 6273	M 19	MW	255.657	-26.268	8.8	1.7	-1.74	13.2	26	79	16.8	1.16	5.9	4.8	H	DeA05	H
NGC 6284		MW	256.119	-24.765	15.3	7.5	-1.26	12.0	4	40	16.4	0.86	5.4	4.6	H	DeA05	H
NGC 6293		MW	257.542	-26.582	9.5	1.9	-1.99	13.0	3	53	15.7	1.10	5.3	4.4	H	Me05	H
NGC 6304		MW	258.634	-29.462	5.9	2.3	-0.45	12.8	13	85	17.2	1.65	5.1	4.3	H	Do10	H
NGC 6316		MW	259.155	-28.140	10.4	2.6	-0.45	-	10	39	17.4	1.65	5.6	4.6	H	-	H
NGC 6333	M 9	MW	259.797	-18.516	7.9	1.7	-1.77	-	27	58	17.4	1.16	5.4	4.4	H	-	H
NGC 6342		MW	260.292	-19.587	8.5	1.7	-0.55	12.5	3	44	17.0	1.40	4.8	3.9	H	DeA05	H
NGC 6356		MW	260.896	-17.813	15.1	7.5	-0.40	13.0	14	49	17.0	0.86	5.6	4.9	H	Me05	H
NGC 6352		MW	261.371	-48.422	5.6	3.3	-0.64	12.8	50	123	18.2	0.67	4.8	3.7	H	Do10	H
NGC 6362		MW	262.979	-67.048	7.6	5.1	-0.99	12.5	68	123	19.3	0.27	5.0	3.3	H	Do10	H
NGC 6388		MW	264.072	-44.735	9.9	3.1	-0.55	11.8	7	31	14.5	1.13	6.0	5.3	H	Mil4	H
NGC 6397		MW	265.175	-53.674	2.3	6.0	-2.02	13.5	3	174	15.5	0.55	4.9	3.0	H	Do10	H
NGC 6440		MW	267.220	-20.360	8.5	1.3	-0.36	-	8	29	17.1	3.27	5.7	5.1	H	-	H
NGC 6441		MW	267.554	-37.051	11.6	3.9	-0.46	12.0	8	34	14.9	1.44	6.1	5.5	H	Mil4	H
NGC 6422		MW	270.892	-30.034	7.7	0.6	-1.34	13.7	3	60	15.8	1.47	5.3	4.3	H	Ba09	H
NGC 6528		MW	271.207	-30.056	7.9	0.6	-0.11	11.0	8	23	16.7	1.65	4.9	4.5	H	La14	H
NGC 6541		MW	272.010	-43.715	7.5	2.1	-1.81	13.2	11	64	15.4	0.43	5.6	4.6	H	Do10	H
NGC 6553		MW	272.323	-25.909	6.0	2.2	-0.18	11.0	32	62	18.2	1.92	5.3	4.2	H	Zo01	H
NGC 6569		MW	273.412	-31.827	10.9	3.1	-0.76	-	21	48	18.1	1.62	5.5	4.5	H	-	H
NGC 6584		MW	274.657	-52.216	13.5	7.0	-1.50	12.2	16	44	17.6	0.31	5.3	4.3	H	Do10	H
NGC 6624		MW	275.919	-30.361	7.9	1.2	-0.44	13.0	4	49	15.3	0.86	5.2	4.4	H	Do10	H
NGC 6637	M 69	MW	277.846	-32.348	8.8	1.7	-0.64	12.5	20	50	16.8	0.55	5.3	4.4	H	Do10	H
NGC 6652		MW	278.940	-32.991	10.0	2.7	-0.81	13.2	6	29	16.1	0.27	4.9	4.3	H	Do10	H
NGC 6656	M 22	MW	279.100	-23.905	3.2	4.9	-1.70	13.5	80	202	17.4	1.04	5.6	3.7	H	Mil4	H
NGC 6681	M 70	MW	280.803	-32.292	9.0	2.2	-1.62	13.0	2	43	14.2	0.21	5.1	4.3	H	Do10	H
NGC 6715	M 54	MW	283.764	-30.480	26.5	18.9	-1.49	13.2	5	49	14.8	0.46	6.2	5.7	H	Mil4	H
NGC 6717	Pal 9	MW	283.775	-22.701	7.1	2.4	-1.26	13.0	5	41	16.8	0.67	4.5	3.8	H	Do10	H
NGC 6723		MW	284.888	-36.632	8.7	2.6	-1.10	12.8	50	92	18.1	0.15	5.4	3.9	H	Do10	H
NGC 6752		MW	287.717	-59.985	4.0	5.2	-1.54	12.5	10	115	14.9	0.12	5.3	4.2	H	Do10	H
NGC 6809	M 55	MW	294.999	-30.965	5.4	3.9	-1.94	13.5	108	170	19.4	0.24	5.3	3.0	H	Do10	H
NGC 6838	M 71	MW	298.444	18.779	4.0	6.7	-0.78	12.5	38	100	19.8	0.76	4.5	2.8	H	Do10	H
NGC 6864	M 75	MW	301.520	-21.921	20.9	14.7	-1.29	11.2	5	28	15.5	0.49	5.7	5.2	H	Me05	H
NGC 6934		MW	308.547	7.404	15.6	12.8	-1.47	12.0	13	41	17.4	0.31	5.2	4.5	H	Do10	H
NGC 7006		MW	315.372	16.187	41.2	38.5	-1.52	12.2	10	26	18.6	0.15	5.3	4.7	H	Do11	H
NGC 7078	M 15	MW	322.493	12.167	10.4	10.4	-2.37	13.2	8	60	14.2	0.31	5.9	5.3	H	Do10	H

**Table 1** – *continued*

ID	Name	Galaxy	RA	Dec	$d_{\odot}$	$d_{gc}$	[Fe/H]	Age	$R_c$	$R_h$	$\mu_{v0}$	$A_v$	GC mass	FoV mass	[Fe/H] source	Age source	Structural source
(1)	(2)	(3)	(4)	(5)	(6)	(7)	(8)	(9)	(10)	(11)	(12)	(13)	(14)	(15)	(16)	(17)	(18)
NGC 7089	M 2	MW	323.363	-0.823	11.5	10.4	-1.65	12.5	19	64	15.8	0.18	5.8	4.9	H	Do10	H
NGC 7099	M 30	MW	325.092	-23.180	8.1	7.1	-2.27	13.2	4	62	15.4	0.09	5.2	4.1	H	Do10	H

*Notes.* Column (1): GC name. Column (2): other common identifiers for GC. Column (3): host galaxy. Columns (4) and (5): right ascension and declination in decimal degrees. Values for MW star clusters are from the 2010 version of the Harris (1996) catalogue, values for other galaxies are from NED. Column (6): heliocentric distance in kpc. For the MW GCs, the distances are from the Harris catalogue. For the Fornax dSph, the LMC and SMC star clusters, we place all star clusters in each galaxy at the same distance, adopting the same distances as McLaughlin & van der Marel (2005), namely 137, 50 and 60 kpc, respectively. Column (7): galactocentric distance in kpc. For MW GCs, the distances are from the Harris catalogue. For the Fornax dSph, the LMC and SMC, we adopt the same distances as McLaughlin & van der Marel (2005), namely 149, 50 and 61 kpc, respectively. Column (8): metallicity in dex. Column (9): age in Gyr. Column (10): projected core radius in arcmin. Column (11): projected half-light radius in arcmin. Column (12): V-band central surface brightness in mag per arcsec<sup>-2</sup>. Column (13): V-band extinction in mag. Column (14): GC log stellar mass in solar masses calculated from the V-band luminosity. Column (15): log stellar mass in solar masses enclosed by the WiFeS field of view calculated from the surface brightness profile. Columns (16), (17) and (18): sources for [Fe/H], age and structural parameters, respectively. References are H: the 2010 version of the Harris (1996) catalogue; Ba09: Barbuy et al. (2009); Ba13: Bastian & Silva-Villa (2013); Co11: Colucci et al. (2011); Dal6: Dalessandro et al. (2016); Da98: Da Costa & Hatzidimitriou (1998); DeA05: De Angeli et al. (2005); Do10: Dotter et al. (2010); Do11: Dotter et al. (2011); F19+G06: Fischer, Welch & Mateo (1992) and Goudfrooij et al. (2006); Ge97: Geisler et al. (1997); Gl08a: Glatt et al. (2008a); Gl08b: Glatt et al. (2008b); Gl09: Glatt et al. (2009); Go06+09: Goudfrooij et al. (2006) and Goudfrooij et al. (2009); Go06+11: Goudfrooij et al. (2006) and Goudfrooij et al. (2011); Go14: Goudfrooij et al. (2014); Gr06: Grocholski et al. (2006); H199: Hill (1999); Jo06: Johnson, Ivans & Stetson (2006); Ke07: Kerber, Santiago & Brocato (2007); La12: Larsen et al. (2012); Lal14: Lagioia et al. (2014); Ma03: Mackey & Gilmore (2003); McL05: McLaughlin & van der Marel (2005); Me05: Meisner & Weiss (2006); Mi14: Milone et al. (2014); Mi98: Mighell, Sarajedini & French (1998); Mu07: Mucciarelli et al. (2007); Mu08: Mucciarelli et al. (2008); Mu10: Mucciarelli et al. (2010); Mu11: Mucciarelli et al. (2011); Mu12: Mucciarelli et al. (2012); Ni15: Niederhofer et al. (2015); O191: Olszewski et al. (1991); O198: Olsen et al. (1998); Or08: Origlia et al. (2008); Pa16: Patrick et al. (2016); S102: Sirianni et al. (2002); Vi07: Villanova et al. (2007); Zo01: Zoccali et al. (2001); deB16: de Boer & Fraser (2016).

radius of the WiFeS field of view (17.4 arcsec). Our observations extend to between 0.12 (NGC 5139) and 13 (Fornax 5) core radii with a median of 1.7 (1.3 for MW GCs) and to between 0.06 (NGC 5139) and 3.7 (Fornax 4) half-light radii with a median of 0.37 (0.32 for MW GCs). We note that previous integrated light studies of MW GCs (e.g. Puzia et al. 2002; Schiavon et al. 2005; Colucci et al. 2017) were also typically limited to within a core radius.

The aperture bias affecting the WAGGS spectra is a concern for a few reasons. First, in the case where the WiFeS field of view covers only a small fraction of a GC's area, stochastic effects could prevent the proper sampling of all stages of stellar evolution. This can be seen in the images of NGC 6121 in Fig. 2 and is especially a concern for lower mass clusters. Secondly, GCs are affected by mass segregation as more massive stars sink to their cluster centres due to dynamical evolution. This causes the slope of the mass function to vary with radius (e.g. Rood et al. 1999; Lee et al. 2003; Andreuzzi et al. 2004; Beccari et al. 2015), which mimics the effect of the IMF varying weakly with radius. Thirdly, the ratio of first- to second-generation stars is observed to vary with radius in some GCs (e.g. Lardo et al. 2011; Larsen et al. 2015). This creates radial gradients in the mean chemical abundances. The latter two effects can be accounted for in comparison with stellar population synthesis models if the mass function and the chemical abundance distributions are known for the same region as the WiFeS field of view, but remain an issue for comparisons with extragalactic GCs. We aim to explore the importance of these effects with our data in future works.

While our sample is subject to observational biases, it is the largest yet sample of integrated spectra of MW GCs. The sample spans the full range of MW GCs metallicities ( $-2.4 < [\text{Fe}/\text{H}] < -0.1$ ) and a wide range of ages (20 Myr to 13.5 Gyr). The sample includes MW GCs from within a kpc of the Galactic Centre (NGC 6528) to nearly 40 kpc out in the MW halo (NGC 7006) as well as 22 GCs in MW satellites.

### 3 OBSERVATIONS AND DATA REDUCTION

We used the WiFeS integral field spectrograph (Dopita et al. 2007, 2010) on the ANU 2.3 m telescope at the Siding Spring Observatory to observe the centres of 86 GCs in the MW and its satellite galaxies. WiFeS uses an image slicer to reformat the telescope image into 25 slices, each 1 arcsec wide and 38 arcsec long on the detector. This gives WiFeS a field of view of  $38 \times 25$  arcsec, which is similar to the median core radius of an MW GC (20 arcsec, 2010 edition of Harris 1996). The light from the image slicer is directed through a beam splitter to the red and blue arms of the spectrograph. Each arm of the spectrograph uses a volume-phase holographic grating to disperse each slice as a long slit spectrum on a  $4096 \times 4096$  pixel e2v CCD with 15  $\mu\text{m}$  pixels. The plate scale in the spatial direction is 0.5 arcsec per pixel, so we binned every two spatial pixels to generate 1 by 1 arcsec spaxels. We observed a single central pointing for each GC with two grating setups. In one, we used the U7000 and R7000 gratings with the RT480 beam splitter to cover 3270–4350  $\text{\AA}$  (0.27  $\text{\AA}$  per pixel) and 5280–7020  $\text{\AA}$  (0.44  $\text{\AA}$  per pixel). In the other, we used B7000 and I7000 gratings with the RT615 beam splitter to cover 4170–5540  $\text{\AA}$  (0.37  $\text{\AA}$  per pixel) and 6800–9050  $\text{\AA}$  (0.57  $\text{\AA}$  per pixel). All four gratings give spectral resolutions of  $\delta\lambda/\lambda \sim 6800$  and slightly undersample the line spread function. This corresponds to a velocity dispersion of 19  $\text{km s}^{-1}$ , which is similar to the velocity dispersions of the most massive GCs in the MW and M31 (e.g. Harris 1996; Strader

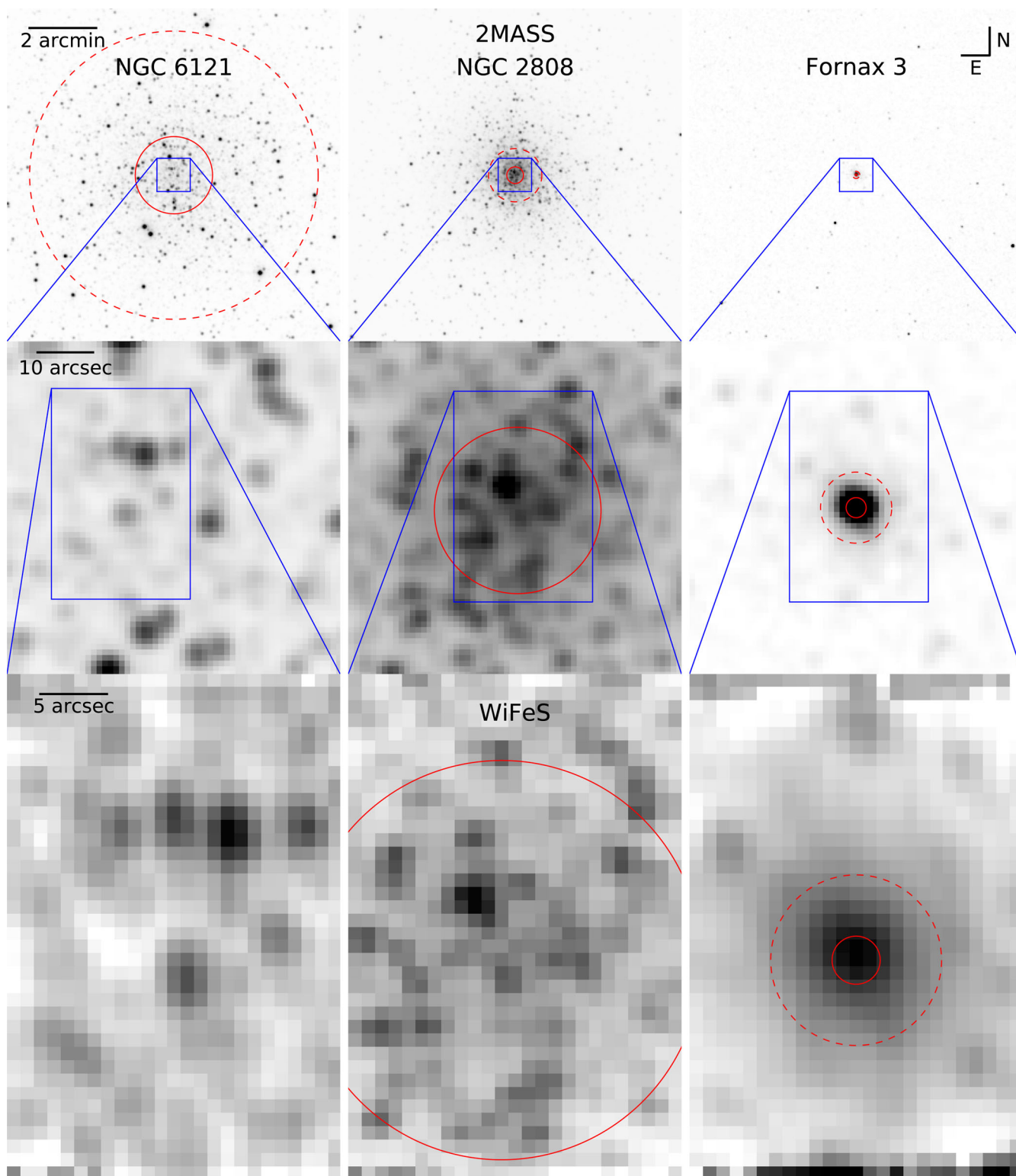


**Figure 2.** Field of view of WAGGS observations. In the top row are 2MASS images for NGC 6121 (M 4, left), NGC 2808 (centre) and Fornax 3 (NGC 1049, right). Each image is  $10 \times 10$  arcmin with north up and east left. In middle row,  $1 \times 1$  arcmin 2MASS images are shown for the same GCs. The footprints of these panels are shown as blue squares in the upper row. In the lower row, the WAGGS I7000 data cubes summed along the spectral direction are shown. The  $25 \times 38$  arcsec footprints of these data cubes are shown as blue rectangles in the middle row. In each panel, the solid red curve shows the core radius while dashed red circle shows the half-light radius. The three GCs pictured span the range of angular sizes in the sample with NGC 6121 being the most extended in our sample, NGC 2808 being close to the median and Fornax 3 being the least extended GC. We note that many of the ‘stars’ in both the 2MASS imaging and the WAGGS cubes are blends of multiple stars.



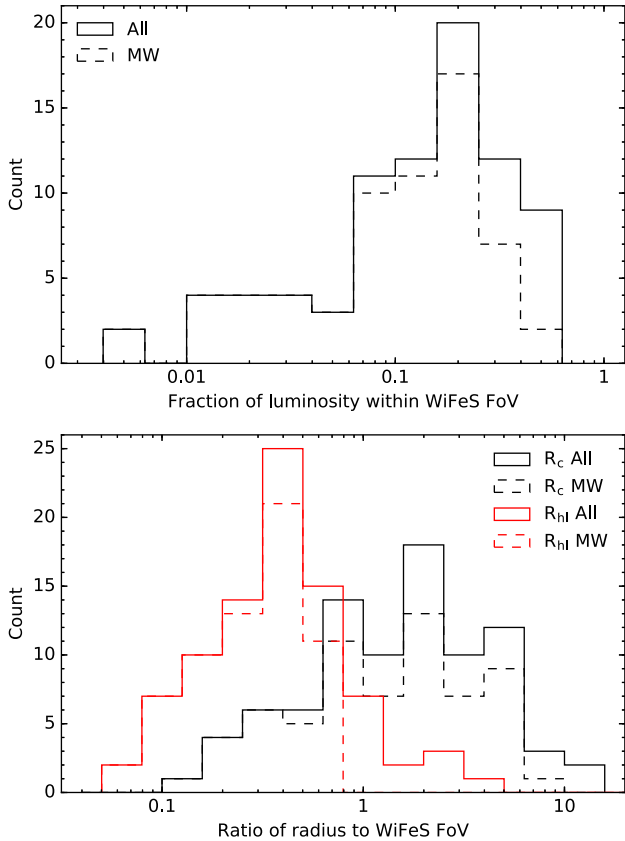


**Figure 3.** Spatial extent of the WAGGS observations. Top: fraction of GC V-band luminosity within the WiFeS field of view. The solid line shows all WAGGS GCs while the dashed line shows only MW GCs. The luminosity within the field of view was calculated by integrating the surface brightness profiles calculated from the structural parameters given in Table 1. Typically, we observe a fraction of 0.19 of the total luminosity of a GC (0.12 in the MW). Bottom: ratio of core radius (black) and half-light radius (red) to the mean radius of the WiFeS field of view (17.4 arcsec). The solid line shows all WAGGS GCs, while the dashed line shows only MW GCs. Typically, we observe out to 1.7 times the core radius and 0.37 times the half-light radius (1.3 and 0.32 times, respectively, for MW GCs).

et al. 2011a). The improvement in spectral resolution over previous studies is illustrated in Fig. 4.

Our observations span 19 nights from 2015 January to 2016 October. Details of the observations are given in the observation log in Table 2, the full version of which is available online as part of the supplementary material. The seeing generally ranged between 1.6 and 2.0 arcsec and conditions were often not photometric.

We used WiFeS in nod-and-shuffle (Glazebrook & Bland-Hawthorn 2001) mode to perform accurate sky subtraction. We observed cycles of 30 s on target and 30 s on sky with the total exposure times estimated from surface brightness profiles calculated from the structural parameters given in Table 1 using the LIMEPY code (Gieles & Zocchi 2015) and a King (1966) profile. Blank patches of sky  $\sim 10$  arcmin (on average 8 half-light radii) from the GC centres were used as the sky fields. Coordinates of the object and sky fields are given in the observing log. We note that we must accurately subtract not only the sky background but also the starlight and nebosity of the host galaxy at the same location as the GC. For GCs in the MW halo, this is not a major issue, while for GCs in the bulge and near the disc of the MW, as well as near the LMC and SMC centres, it can be relevant.

Our usual observing strategy was to take three science exposures with the U7000 and R7000 gratings before exposing a NeAr arc with the same grating setup. We then switched the gratings to B7000 and I7000 and exposed a NeAr arc with the new grating setup before taking three science exposures. We then moved to the next target and took three B7000/I7000 science exposures and a B7000/I7000 arc before reconfiguring the gratings and observing the U7000/R7000 arc and the three U7000/R7000 science exposures. Before each observing night, we observed five bias, lamp flat and wire exposures (to spatially align the instrument) for each of the two grating setups. We also observed sky flat exposures for both grating setups during twilight.

We typically observed a white dwarf and a metal poor red giant each night as spectrophotometric standards. During our 2016 April and 2016 September/October runs, we observed a number of stars from both the MILES spectral library (Sánchez-Blázquez et al. 2006) and the Lick index standard stars (Worthey et al. 1994) to test the reliability of our spectral index measurements. We did not use nod-and-shuffle for either the spectrophotometric standard star observations or the line index standards. Details of the standard star observations are given in the observing log in Table 2.

### 3.1 Data reduction

We used the PYWiFeS (Childress et al. 2014a,b) pipeline to reduce the observations. We provide an outline of the data-reduction procedure performed by PYWiFeS here but refer the interested reader to Childress et al. (2014b) for more details. After performing bias subtraction, the pipeline separates each image into the 25 slitlets with nod-and-shuffle exposures being further divided into sky and object slitlets. For each slitlet, the pipeline calculates spectral flat-field responses using the lamp flats, spatial flat-field responses using the sky flats and wavelength solutions using the arc frames. For each slitlet, the pipeline performs cosmic ray identification and repair using a modified version of LA Cosmic (van Dokkum 2001). For exposures using nod-and-shuffle, each sky slitlet is subtracted from the corresponding object slitlet. Multiple exposures of the same object are combined slitlet by slitlet. After applying the flat-field and wavelength calibrations, the pipeline uses the wire exposures to spatially align the slitlets and corrects for the effects of atmospheric differential refraction using the equations of Filippenko (1982). The pipeline then resamples and combines the observed pixels of each slitlet in to a single rectilinear data cube. The pipeline uses the observed standard stars to flux calibrate the data cubes. When no standard star was observed, we used the star observed on the previous night. For the R7000 and I7000 gratings, the pipeline fits the standard star spectra outside of wavelength regions affected by telluric absorption with a polynomial before using the ratio of the fitted polynomial to the observed standard star spectra to correct each data cube for telluric absorption. We preferred to use the white dwarf standard stars for the telluric corrections, only using the red giant standard stars when no telluric star was observed that night.

We performed astrometry of the data cubes by comparing images created by summing the I7000 cubes along the wavelength direction with the J-band 2MASS (Skrutskie et al. 2006) images. The I7000 cubes were used due to the stronger surface brightness fluctuations signal in the red while 2MASS imaging has similar spatial resolution to the WiFeS data cubes. Accurate astrometry is, however, challenging for these targets, as the field is severely crowded at the effective spatial resolution and field size of the WiFeS IFU.

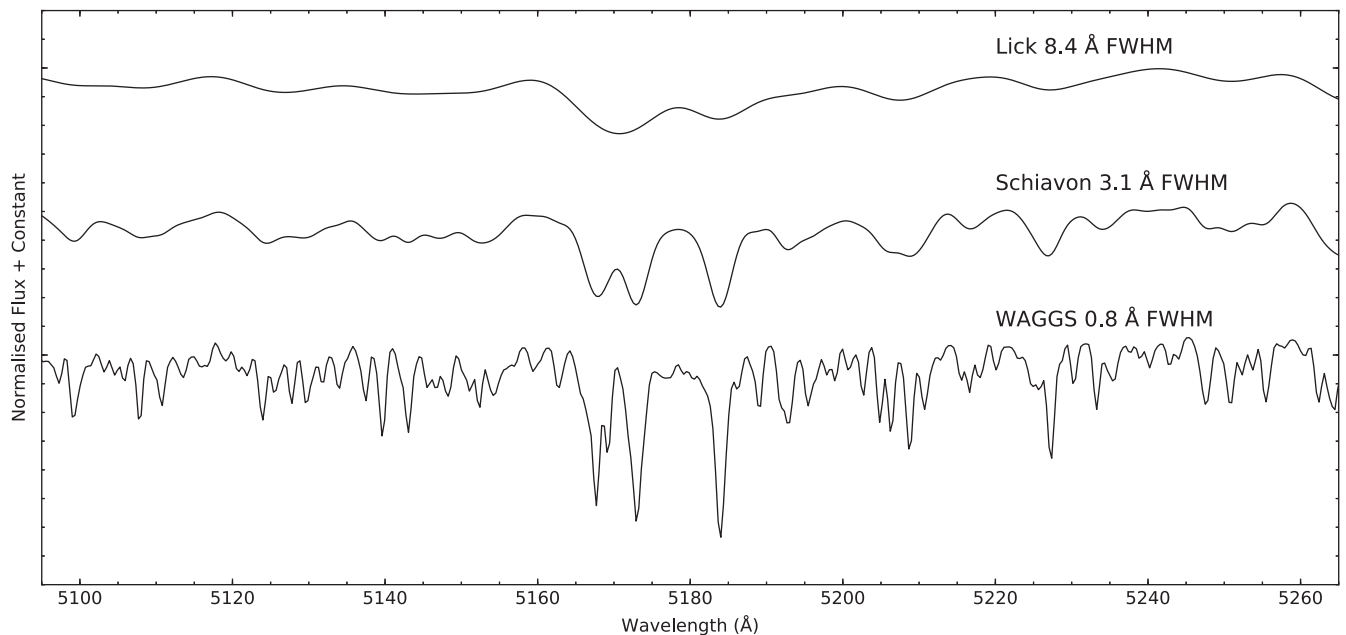


**Figure 4.** WAGGS spectral resolution compared to previous work. Our spectrum of NGC 104 around  $Mg_b$  is plotted at its original spectral resolution ( $R = 6800$ ,  $0.8 \text{ \AA}$  FWHM, bottom), smoothed to the spectral resolution of Schiavon et al. (2005) library of GC spectra ( $R = 1700$ ,  $3.1 \text{ \AA}$  FWHM, middle) and of the Lick index system (Worthey et al. 1994,  $R = 600$ ,  $8.4 \text{ \AA}$  FWHM, top). The smoothed spectra have been offset in flux for legibility. This NGC 104 spectrum has an S/N of  $689 \text{ \AA}^{-1}$ . Our spectra have four times higher spectral resolution compared to the spectra of Schiavon et al. (2005) and 11 times the spectral resolution of the Lick system. This high resolution allows us to study much weaker spectral lines. Note that the apparently smooth pseudo-continuum at low resolution is made up of numerous weak absorption lines.

**Table 2.** Observing log.

ID	Object	Sky	Date	Grating	Exposure [s]	S/N [ $\text{\AA}^{-1}$ ]	Notes
(1)	(2)	(3)	(4)	(5)	(6)	(7)	(8)
NGC 104	00:24:08.2 -72:04:52.1	00:08:51.3 -72:01:55	2015-01-30 10:50:09.5	R7000	240	1145	–
NGC 104	00:24:08.2 -72:04:52.1	00:08:51.3 -72:01:55	2015-01-30 10:50:09.5	U7000	240	264	–
NGC 104	00:24:08.2 -72:04:52.1	00:08:51.3 -72:01:55	2015-01-30 11:13:50.5	B7000	180	689	–
NGC 104	00:24:08.2 -72:04:52.1	00:08:51.3 -72:01:55	2015-01-30 11:13:50.5	I7000	180	911	–
NGC 362	01:03:16.9 -70:51:04.6	01:01:38.1 -70:42:12	2015-01-30 11:40:33.5	B7000	180	338	–
NGC 362	01:03:16.9 -70:51:04.6	01:01:38.1 -70:42:12	2015-01-30 11:40:33.5	I7000	180	470	–
NGC 362	01:03:16.9 -70:51:04.6	01:01:38.1 -70:42:12	2015-01-30 12:17:27.5	U7000	180	91	–
NGC 362	01:03:16.9 -70:51:04.6	01:01:38.1 -70:42:12	2015-01-30 12:17:27.5	R7000	180	487	–
HD 44007	06:18:48.2 -14:50:42	06:18:48.2 -14:50:42	2015-01-30 12:35:09.5	U7000	210	366	flux standard
HD 44007	06:18:48.2 -14:50:42	06:18:48.2 -14:50:42	2015-01-30 12:35:09.5	R7000	210	904	flux standard
HD 44007	06:18:48.2 -14:50:42	06:18:48.2 -14:50:42	2015-01-30 12:59:20.5	I7000	180	774	flux standard
HD 44007	06:18:48.2 -14:50:42	06:18:48.2 -14:50:42	2015-01-30 12:59:20.5	B7000	180	732	flux standard
...	...	...	...	...	...	...	...

*Notes.* The full version of this table is provided in a machine readable form in the online Supporting Information. Column (1): GC or star. Column (2): object coordinate. Column (3): sky coordinate. Column (4): observation date and UTC time. Column (5): grating. Column (6): exposure time in seconds. Column (7): mean S/N per  $\text{\AA}$  for the integrated spectra. For the U7000 grating, this was measured between 4000 and 4050  $\text{\AA}$ ; for the B7000 grating, between 4800 and 4850  $\text{\AA}$ ; for the R7000 grating, between 6400 and 6450; for the I7000 grating, between 8400 and 8450  $\text{\AA}$ .

### 3.2 Integrated spectra

For most of the GCs in our sample, the WiFeS field of view is smaller than their half-light diameter. For these objects, we created integrated spectra by simply summing the spatial pixels, excluding the first two and last two rows of cubes as these are noisier (these rows come from the ends of each slice) and show larger residuals from the subtraction of sky emission lines. For the small number of GCs with half-light diameters smaller than the instrument field of view (namely the three GCs in Fornax, NGC 416 in the SMC, NGC 1786, NGC 1868, NGC 1916, NGC 2004 and NGC 2136 in

the LMC), we created integrated spectra by summing all the spatial pixels within their half-light radii.

For each integrated spectrum, we calculated the mean S/N in a grating-dependent wavelength region. The wavelength regions, minimum, median and maximum S/N are given for each grating in Table 3, while the S/N distributions are plotted in Fig. 5. The S/N for each observation are given in Table 2. Generally, the U7000 grating has the worst S/N and the R7000 and I7000 gratings the best. Since exposure times were calculated using the  $V$ -band surface brightnesses, metal-rich GCs and GCs with more foreground extinction generally have lower S/N at bluer wavelengths. Except

**Table 3.** Signal-to-noise ratios.

Grating	$\lambda_{\min}$ Å	$\lambda_{\max}$ Å	$S/N_{\min}$ Å <sup>-1</sup>	$S/N_{\text{med}}$ Å <sup>-1</sup>	$S/N_{\max}$ Å <sup>-1</sup>
(1)	(2)	(3)	(4)	(5)	(6)
U7000	4000	4050	0.3	29	264
B7000	4800	4850	4.4	77	689
R7000	6400	6450	1.2	161	1145
I7000	8400	8450	7.9	157	911

*Notes.* Column (1): grating. Column (2): minimum wavelength of S/N calculation region. Column (3): maximum wavelength of S/N calculation region. Column (4): minimum S/N per Å. Column (5): median S/N per Å. Column (6): maximum S/N per Å.

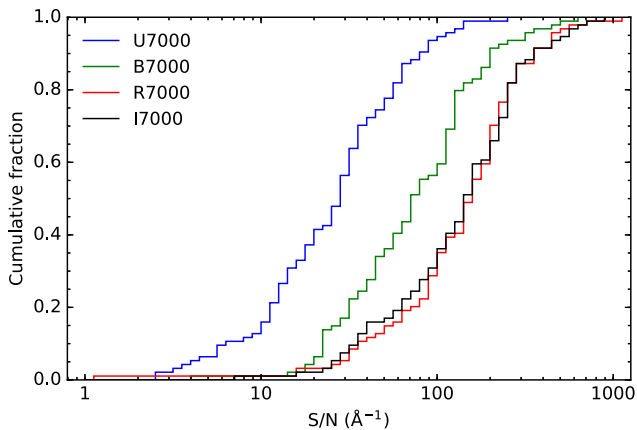


**Figure 5.** Cumulative S/N per Å distributions of the integrated spectra for each of the gratings. In general, the S/N of the U7000 spectra is lower than that of the B7000 spectra while the R7000 and I7000 are higher.

for the U7000 grating and wavelength regions affected by strong sky emission lines or telluric absorption, S/N generally does not vary dramatically within a grating. In the case of the U7000 grating, the S/N increases significantly at shorter wavelengths. The S/N of spectra of GCs in the MW satellites are generally lower than those in the MW with the median B7000 S/N being 115 Å<sup>-1</sup> in the MW and 46 Å<sup>-1</sup> in the MW satellites.

The integrated spectra of NGC 104 across the entire observed wavelength range are shown in Fig. 6. This illustrates the wide wavelength coverage of the WAGGS spectra that cover a wide range of spectral features including molecular bands in the near-UV, the traditional Lick (Worthey et al. 1994) indices, the sodium doublets at 5895 and 8910 Å, H $\alpha$  and the CaT. Integrated spectra of GCs with a range of metallicities in the spectral region of H $\beta$  and Mg $_b$  are shown in Fig. 7 and around the CaT in Fig. 8. Unsurprisingly, in both figures a range of metal lines increases in strength with increasing metallicity. The shape of the pseudo-continuum also becomes redder with increasing metallicity although we note that we have not corrected our spectra for the effects of extinction and that our more metal-rich GCs generally have higher foreground reddening than our metal-poor GCs. The strength of H $\beta$  decreases with increasing metallicity whereas in the CaT region, weak Paschen absorption is only seen at the lowest metallicities. Integrated spectra of GCs with a range of ages in the spectral region of H $\beta$  and Mg $_b$  are shown in Fig. 9 and around the CaT in Fig. 10. As expected, the strength H $\beta$  decreases with increasing age while the strength of metal lines increases with age. In the region of the CaT, strong Paschen absorption is seen only in GCs younger than 1 Gyr.

### 3.3 Repeated observations

In several cases, we observed the same GC more than once with the same grating setup. Often this occurred when we were only able to observe one grating setup for a GC on a given night; when revisiting those GCs in order to complete the observations, we usually elected to observe both grating setups. In some cases, poor data quality prompted us to reobserve a particular GC. We intentionally reobserved NGC 2808 and NGC 7099 to assess the repeatability of our observations. We have repeated observations of the U7000 and R7000 gratings for NGC 2808, NGC 3201, NGC 5286, NGC 6304, NGC 6723 and NGC 7099 and of the B7000 and I7000 gratings for NGC 1846, NGC 2808, NGC 6284, NGC 6304, NGC 6342, NGC 6717 and NGC 7099.

We show a comparison of our NGC 2808 integrated spectra for two different nights (2015-01-31 and 2015-07-09) across the entire R7000 grating in Fig. 11 and over a narrower wavelength range in Fig. 12. Since the declinations of the two observations differ by 3 arcsec, for this comparison, we extracted spectra from spaxels that cover the same area on sky. Over the entire grating, the flux calibration is generally consistent between observations to within a couple percent. The largest variance in the ratio of the two nights' spectra is seen over wavelength regions such as redwards of 6875 Å and around 6280 Å, which are affected by telluric absorption. For wavelength ranges of  $\sim 100$  Å or less, the differences between observations are generally consistent with the uncertainties provided by the PyWiFeS pipeline modulo a multiplicative factor in flux. We see similar differences with the other gratings and other GCs, although we note that the quality of the flux calibration is poorer with the U7000 grating. We believe that the PyWiFeS flux calibration procedure is responsible most of the systematic differences between repeated observations. We aim to improve upon the flux calibration in future work.

We also note that due to effects of variable stars, in particular long period variables, the integrated light of GCs is intrinsically variable at the percent level on the time-scale of hours to years (Conroy, van Dokkum & Choi 2015). This effect is most noticeable in spectral features such as the TiO bands that are predominantly formed in the coolest, brightest giants. We were able to trace a one percent difference between our two R7000 observations of NGC 2808 (observed 159 d apart) to three known (Lebzelter & Wood 2011) long period variables in our field of view.

### 3.4 Resolved stars and stochastic sampling

As can be seen in Fig. 2, individual stars can be seen in the data cubes of the closest or lowest surface brightness GCs. In Figs 13 and 14, we compare our WiFeS data cubes with *HST*/ACS imaging from the ACS Globular Cluster Treasury Survey (Sarajedini et al. 2007), downloaded from the Hubble Legacy Archive.<sup>1</sup> In each of these figures, we also show the colour–magnitude diagrams ( $F606W \sim V$ ,  $F814W \sim I$ ) for all stars in the ACS Globular Cluster Treasury Survey catalogues (Anderson et al. 2008) and those stars within the WiFeS field of view. For NGC 6121, the brightest star in the WiFeS field of view is an  $F814W=10.97$  red giant while the faintest identifiable stars are  $F814W \sim 15$  subgiant branch stars. We note that many of the ‘stars’ in the WiFeS cubes are in fact blends of multiple stars. As can be seen in the lower panel of Fig. 13, the colour–magnitude diagram of NGC 6161 is not well sampled with only

<sup>1</sup> <http://hla.stsci.edu/>.

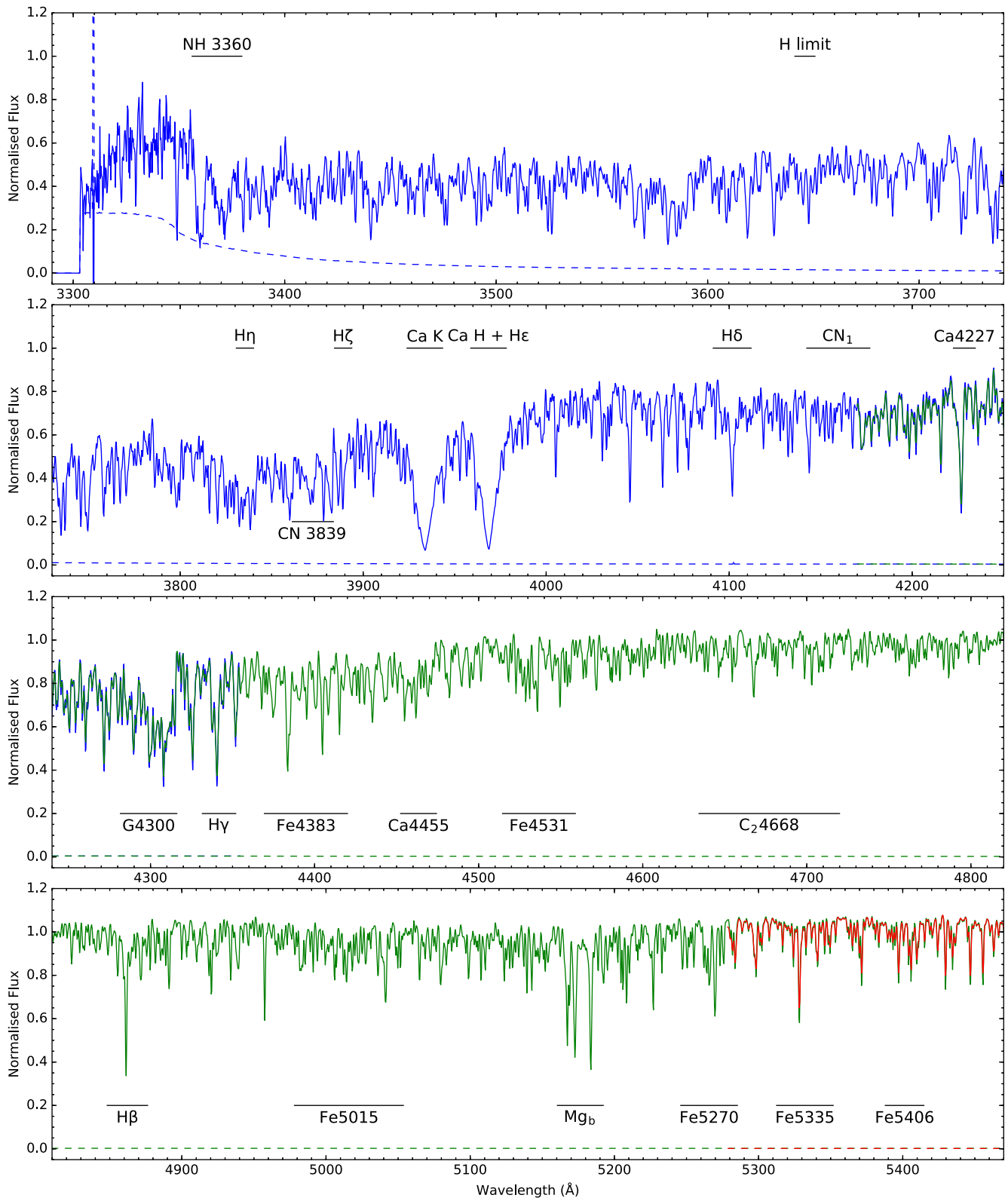


**Figure 6.** WAGGS spectra of NGC 104. The U7000 grating spectrum is shown in blue, the B7000 spectrum in green, the R7000 in red and the I7000 in black. For each grating, the uncertainties provided by the PyWiFeS pipeline are shown as a dashed line. Commonly used spectral indices are shown as black horizontal lines. Grey-shaded regions denote wavelength regions where telluric lines have been corrected by the PyWiFeS pipeline. The spectra have been shifted to the restframe and normalized such that the average flux in the wavelength range 5300–5500 Å is unity and that the average flux in the regions of overlap is the same for both gratings.

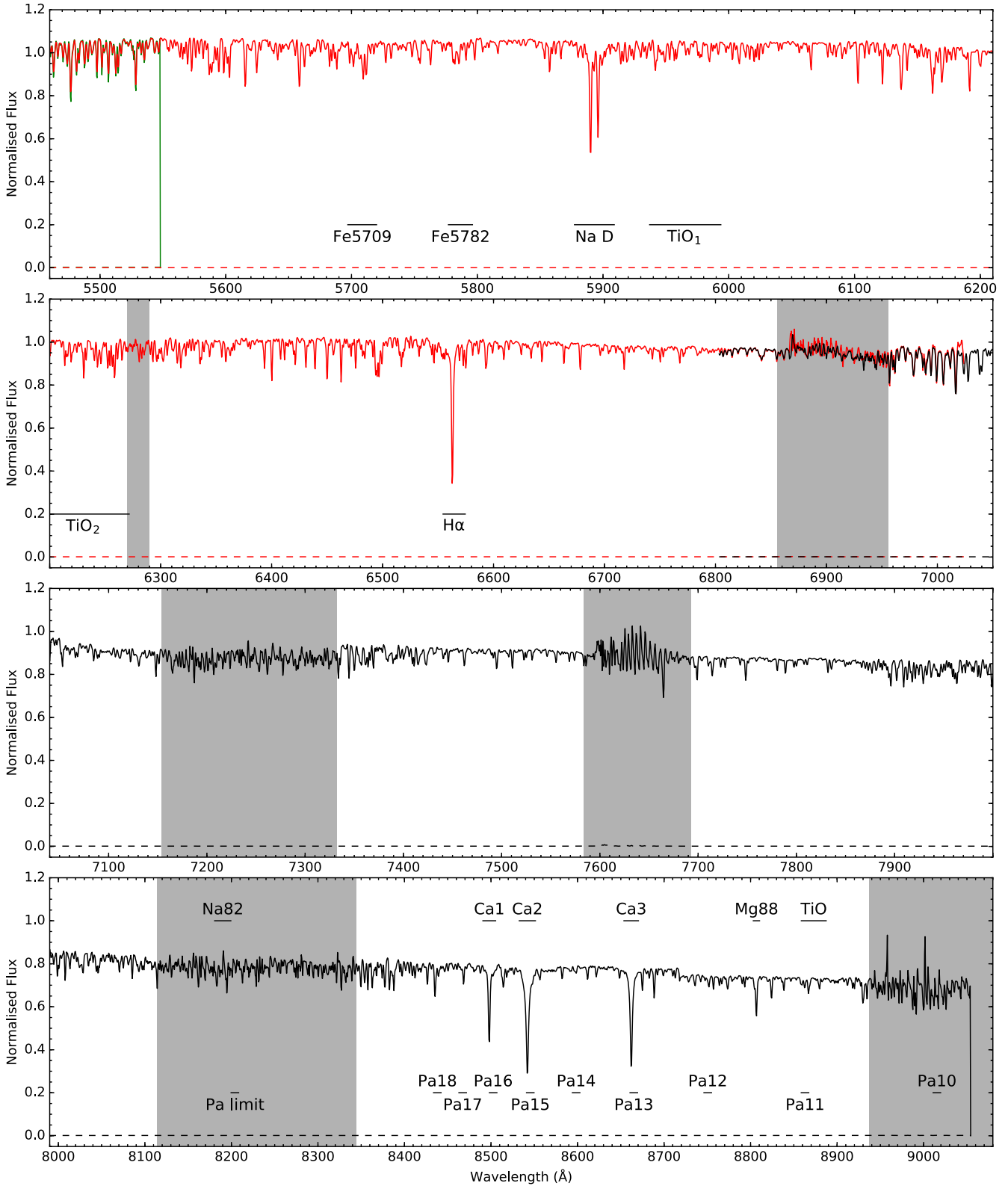
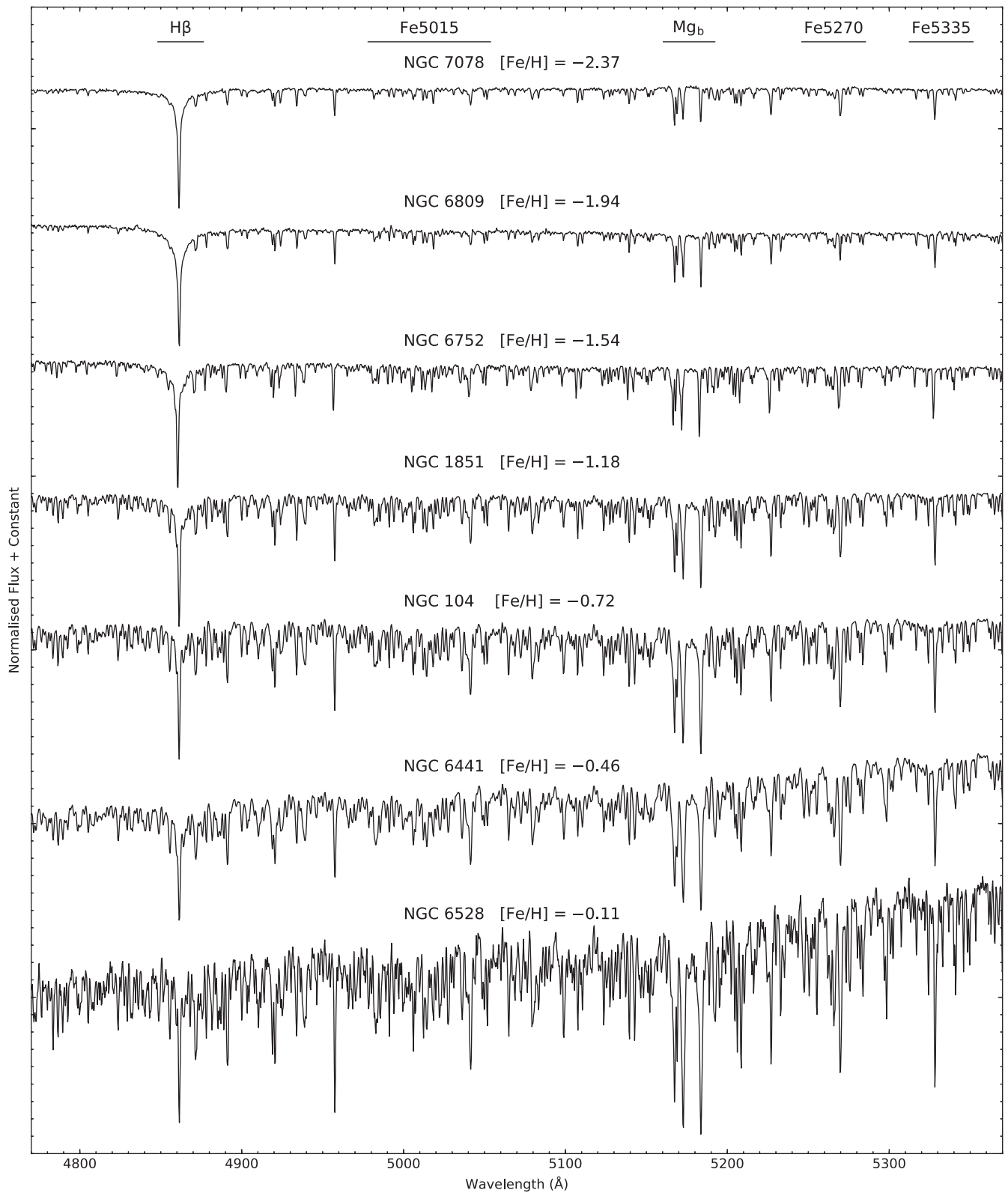


Figure 6 – continued

one red giant branch star brighter than the horizontal branch in the WiFeS field of view. The colour–magnitude diagram of NGC 2808 (Fig. 14), however, is well sampled by the WiFeS field of view. We note that NGC 2808 is close to the median of our sample in

terms of distance from Sun and at the 80th percentile of the *V*-band luminosity enclosed by the WiFeS field of view while NGC 6121 is the closest GC in our sample and has the fourth lowest enclosed luminosity.



**Figure 7.** WAGGS spectra in the region of  $H\beta$  and  $Mg_b$  for GCs with a range of metallicities. The spectra increase in metallicity from top to bottom and have been offset an arbitrary amount in the y-axis. The GCs plotted in this figure span the range of metallicities in the WAGGS sample and are all old (age  $> 10$  Gyr). A whole host of metal lines increases in strength with metallicity while  $H\beta$  decreases.

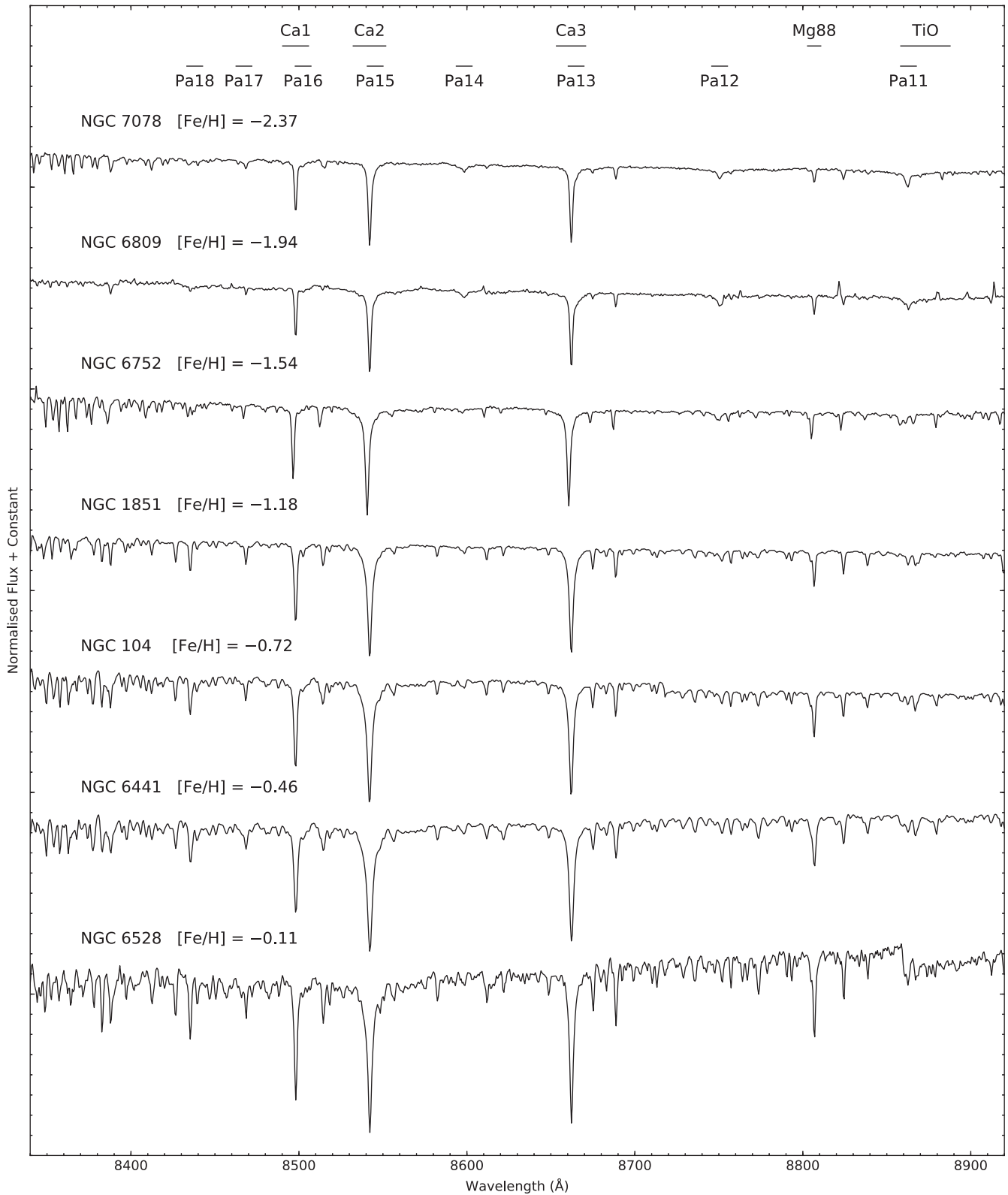


**Figure 8.** The WAGGS spectra in the region of the CaT for GCs with a range of metallicities. The spectra increase in metallicity from top to bottom and have been offset an arbitrary amount in the y-axis. The GCs plotted in this figure span the range of metallicities in the WAGGS sample and are all old (age > 10 Gyr). Weak Paschen line absorption is visible only in the lowest metallicity GCs, while the TiO bandhead at 8860 Å appears only at high metallicity.

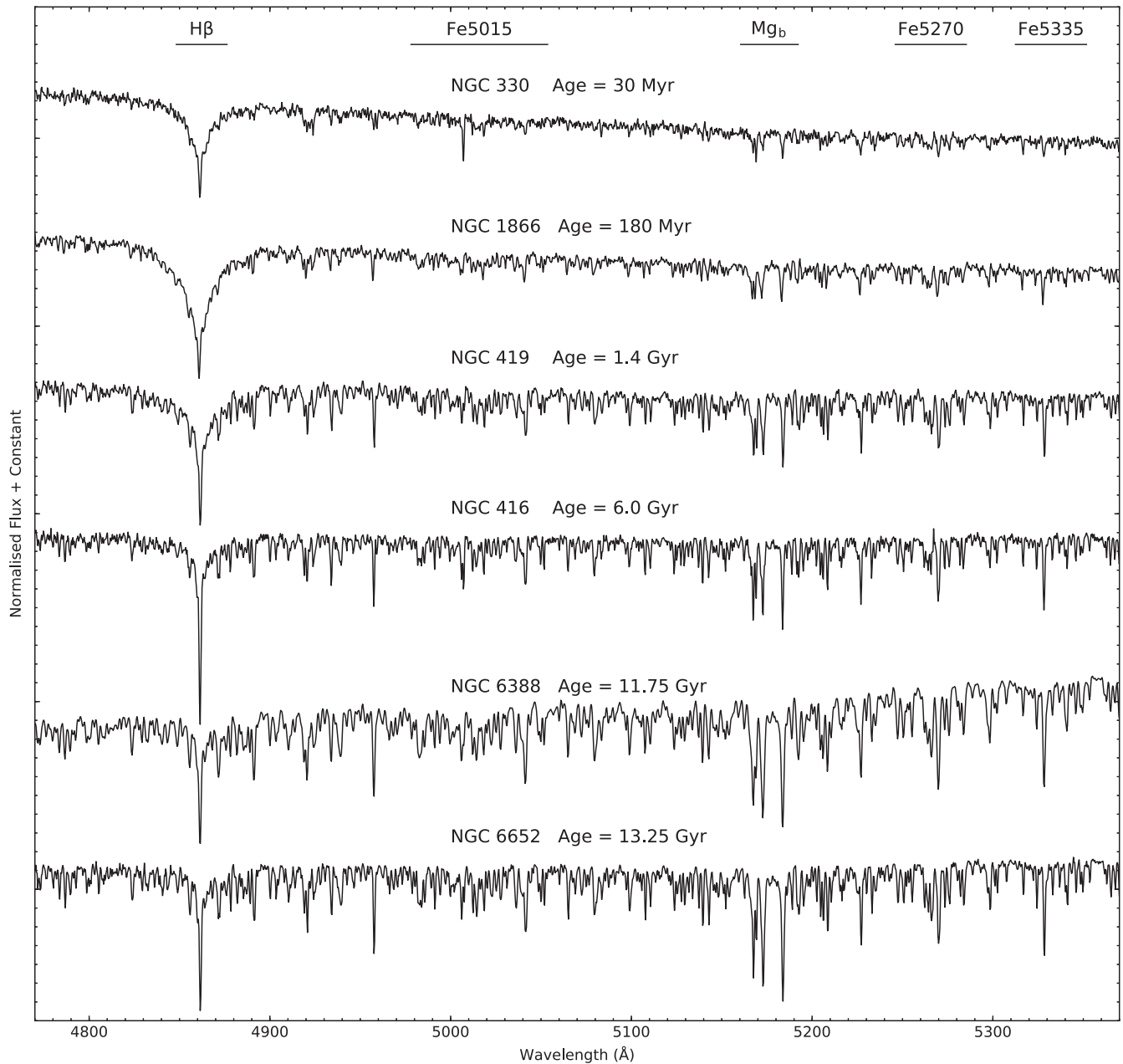


**Figure 9.** The WAGGS spectra in the region of H  $\beta$  and Mg $_b$  for GCs with a range of ages. The spectra increase in age from top to bottom and have been offset an arbitrary amount in the y-axis. The GCs plotted in this figure span the range of ages in the WAGGS sample and have been selected to fall in the metallicity range  $-1 < [\text{Fe}/\text{H}] < -0.4$ . Going from young ages to old, the strength of H  $\beta$  decreases and the strength of metal lines increases.

To assess what effect this stochastic sampling of the colour–magnitude diagrams has on the integrated spectra, we divided our data cubes of NGC 2808 and NGC 6121 each in two and extract spectra for each half cube. As can be seen in Fig. 15, the differences between the two halves of the data cube are large for NGC 6121 while for NGC 2808, the differences are small but significant. The effects of stochastic sampling are largest for the closest GCs and for the GCs with lowest enclosed luminosity. Stochastic sampling of the IMF is also an issue for the younger LMC and SMC GCs as their integrated light can be dominated by a handful of supergiants or thermally pulsing asymptotic giant stars. The effects of stochastic sampling are generally larger than the statistical uncertainty of the integrated spectra but are wavelength and spectral feature de-

pendent, with spectral features produced by rare but luminous stars, such as TiO bands produced by cool giants, showing the largest variability.

### 3.5 First data release

The integrated spectra of the WAGGS sample are available at <http://www.aao.gov.au/surveys/waggs>. We note that in this first data release, spectra have been flux calibrated only in a relative sense. Future data releases will include the full data cubes, improved flux calibration and improved telluric corrections. We also aim to enlarge our sample with further observations of MW, LMC and SMC GCs.



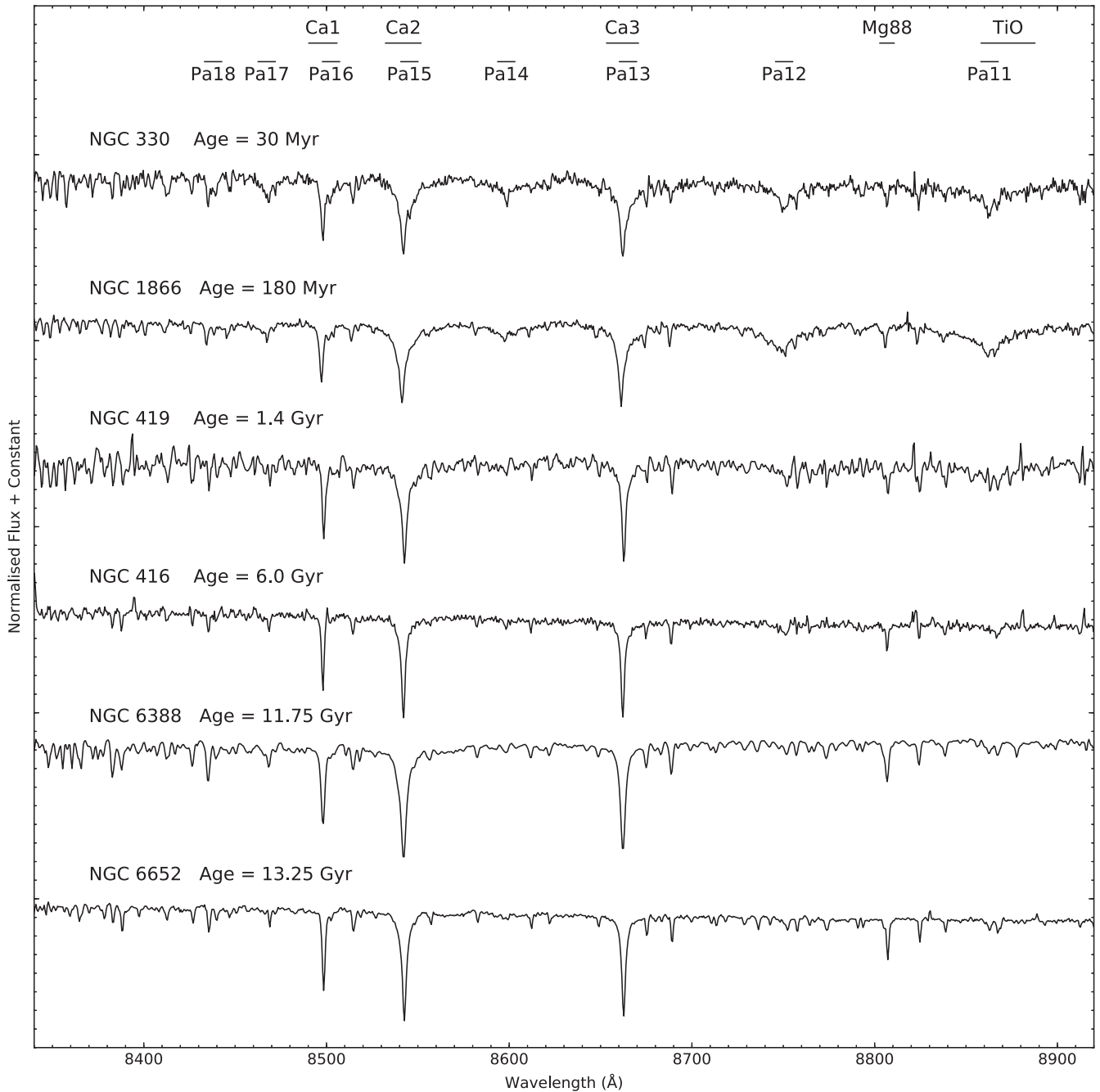


**Figure 10.** The WAGGS spectra in the region of the CaT for GCs with a range of ages. The spectra increase in age from top to bottom and have been offset an arbitrary amount in the y-axis. The GCs plotted in this figure span the range of ages in the WAGGS sample and have been selected to fall in the metallicity range  $-1 < [\text{Fe}/\text{H}] < -0.4$ . Note the presence of Paschen absorption only in the youngest GCs.

#### 4 SUMMARY AND FUTURE WORK

We have presented WAGGS, a new library of integrated GC spectra. We have used the WiFeS integral field spectrograph to observe the centres of 64 MW, 14 LMC, 5 SMC and 3 Fornax dSph GCs. As can be seen in the lower left panel of Fig. 1 and Figs 7–10, our sample spans a wide range of metallicities ( $-2.4 < [\text{Fe}/\text{H}] < -0.1$ ) and ages (20 Myr to 13.5 Gyr). The WAGGS spectra have significantly higher spectral resolution ( $R = 6800$ ) compared to earlier studies

(Fig. 4) while Fig. 6 demonstrates the wide wavelength coverage (3300–9050 Å) of our spectra.

The WAGGS data set will be quite useful for a range of applications in Galactic and extragalactic astronomy. The most obvious use is testing stellar population synthesis models. We note that the spectral resolution and wavelength coverage of the WAGGS spectra exceed those of the commonly used MILES (Sánchez-Blázquez et al. 2006) empirical stellar library. The spatially resolved nature of the WAGGS data cubes makes possible for the stars contributing

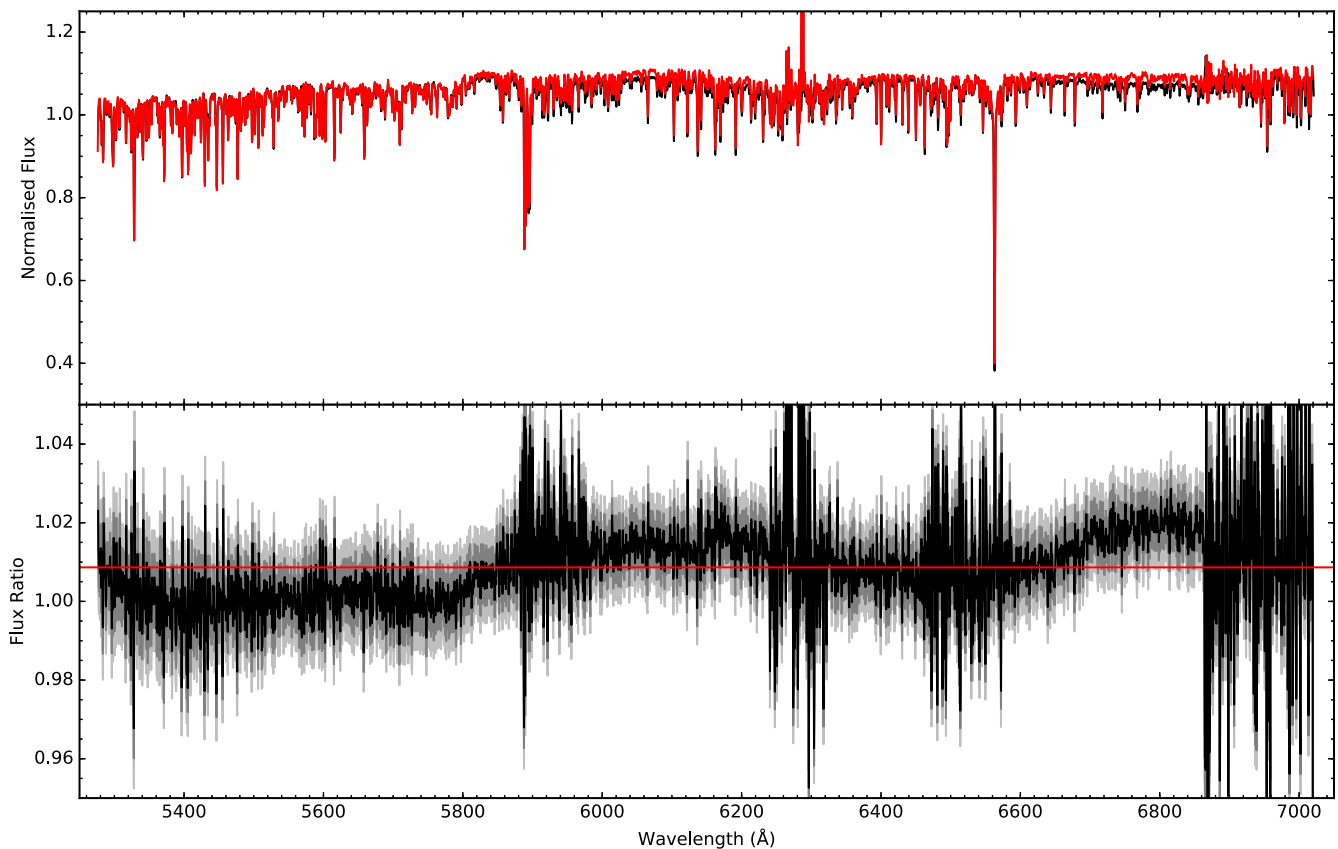


**Figure 11.** Top: comparison of the R7000 integrated spectra of NGC 2808 from 2015-01-31 (black) and from 2015-07-09 (red). This is a relative comparison as both observations have been normalized such that their mean flux between 5300 Å and 5500 Å is unity. The 2015-01-31 spectrum has an S/N of  $744 \text{ \AA}^{-1}$  while the 2015-07-09 spectrum has an S/N of  $389 \text{ \AA}^{-1}$ . These S/N are based on the uncertainties provided by the PyWiFeS pipeline. The spectra have been shifted to the rest frame. Bottom: ratio of the two nights observations in black. The dark grey and light grey regions show the  $1\sigma$  and  $2\sigma$  uncertainties in the ratio. We note that the regions of greatest variance — 5880–5980 Å, 6270–6330 Å, 6460–6580 Å and redwards of 6860 Å — lie in wavelength regions affected by telluric lines.

to the integrated spectra to be identified in resolved imaging. This allows the luminosity function from high spatial resolution imaging of the same area on the sky (e.g. *HST*-based photometry) to be used in place of an assumed IMF. The WAGGS spectra enable comparisons of measurements of IMF sensitive spectral features such as the sodium doublet at 8190 Å and the CaT with models. The effects of GC dynamical evolution, namely mass segregation, could be used to provide stellar populations with the same ages and chemical compositions but different present-day mass functions.

The data set will also make possible the testing of a range of stellar population analysis techniques, including spectral indices (e.g. Worthey 1994; Gallazzi et al. 2006; Schiavon 2007; Graves & Schiavon 2008), full spectral fitting (e.g. Koleva et al. 2008; Conroy, Graves & van Dokkum 2014) and spectral synthesis of narrow spectral regions (e.g. Colucci et al. 2009; Larsen et al. 2012; Sakari et al. 2013) as well as hybrid techniques (e.g. template-based measurements of the CaT, Foster et al. 2010; Usher et al. 2012). The semiresolved nature of many of the data cubes can be used to test novel semiresolved stellar population analysis techniques (e.g. van Dokkum & Conroy 2014; Conroy & van Dokkum 2016). WAGGS spectra can also be used to derive empirical relations between spectral indices and param-

eters such as metallicity (e.g. Brodie & Huchra 1991; Strader & Brodie 2004; Sinnott et al. 2010), horizontal branch morphology (e.g. Schiavon et al. 2004) or blue straggler frequency (Cenarro et al. 2008). The Local Group GCs in WAGGS can now be compared in a model independent way with observations of extragalactic GCs.

The WAGGS spectra will also be a boon to studies of the GCs of the MW and its satellites. Our current sample covers 40 per cent of the MW’s GC system. The high-S/N, intermediate-resolution spectra may be used to generate a homogeneous abundance scale based on a large number of GCs, in both the MW and its satellites. Since the velocity resolution of the WiFeS spectra ( $\sigma = 19 \text{ km s}^{-1}$ ) is comparable to the central velocity dispersion of the more massive GCs, the WAGGS data cubes should provide useful constraints to dynamical modelling. Improved dynamical GC masses at high metallicities and at younger ages would allow a better understanding of how the  $M/L$  varies with age and metallicity. In future, we plan on exploring the use of point spread function fitting to extract spectra of individual stars from our data cubes in a manner analogous to point spread function photometry (e.g. Roth et al. 2004; Kamann, Wisotzki & Roth 2013; Pastorello et al. 2013; Husser et al. 2016).

The WAGGS spectra will be extremely useful to test stellar population synthesis models and analysis techniques, to compare with

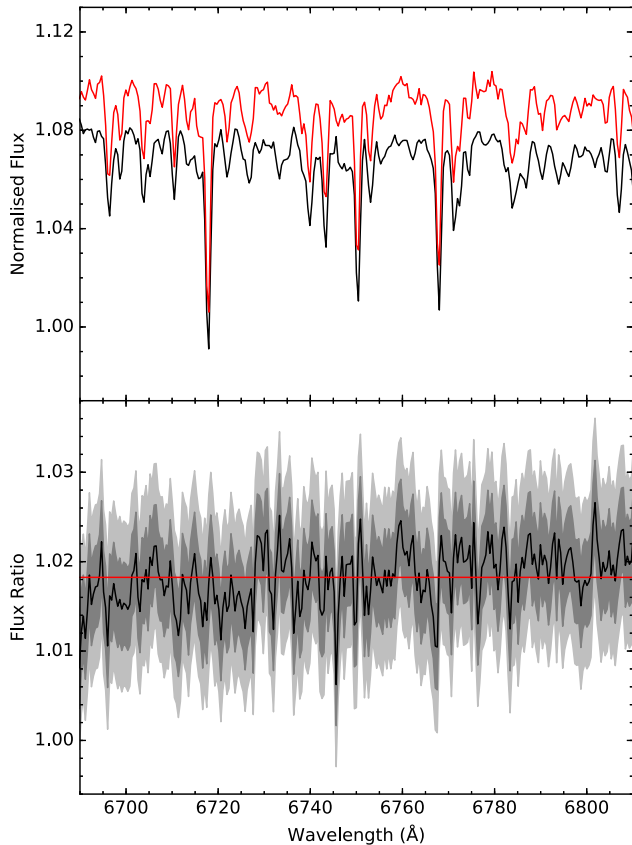


**Figure 12.** Top: comparison of the R7000 spectra of NGC 2808 from 2015-01-31 (black) and from 2015-07-09 (red) over a narrower wavelength range than Fig. 11. As before the spectra have been normalized to unity in the wavelength range of 5300–5500 Å and shifted to the rest frame. Bottom: ratio of the two nights observations in black. The dark grey and light grey regions show the  $1\sigma$  and  $2\sigma$  uncertainties in the ratio. Modulo an  $\sim 1$  per cent difference in flux calibration, the spectra from the two nights show excellent agreement within the uncertainties provided by the PyWiFeS pipeline.

extragalactic GC observations and to study the sample GCs themselves. We have made the first data release of the integrated spectra publicly available on the project website. Future papers in this series will focus on using the WAGGS data set to address a number of scientific questions.

## ACKNOWLEDGEMENTS

We thank the referee Søren Larsen for his useful comments and suggestions that helped to improve this paper. We also thank Nate Bastian, Joel Pfeffer and Thomas Beckwith for helpful discussions and useful suggestions. We are grateful to Paolo Bonfini, Martina Fagioli, Bililign Dullo, Elisa Boera, Srdan Kotus and Paul Frederic Robert for their assistance with the observations. We thank Simon O’Toole for his assistance with hosting the first WAGGS data release. We also wish to greatly thank the Siding Spring Observatory staff for their assistance with the ANU 2.3 m telescope and WiFeS instrument. We also wish to thank Jeremy Mould for originally suggesting the use of WiFeS to obtain integrated spectra of Local Group GCs. CU wishes to thank the University of Victoria’s Department of Physics and Astronomy for their hospitality while a portion of this work was carried out. CU gratefully acknowledges financial support from the European Research Council (ERC-CoG-646928,

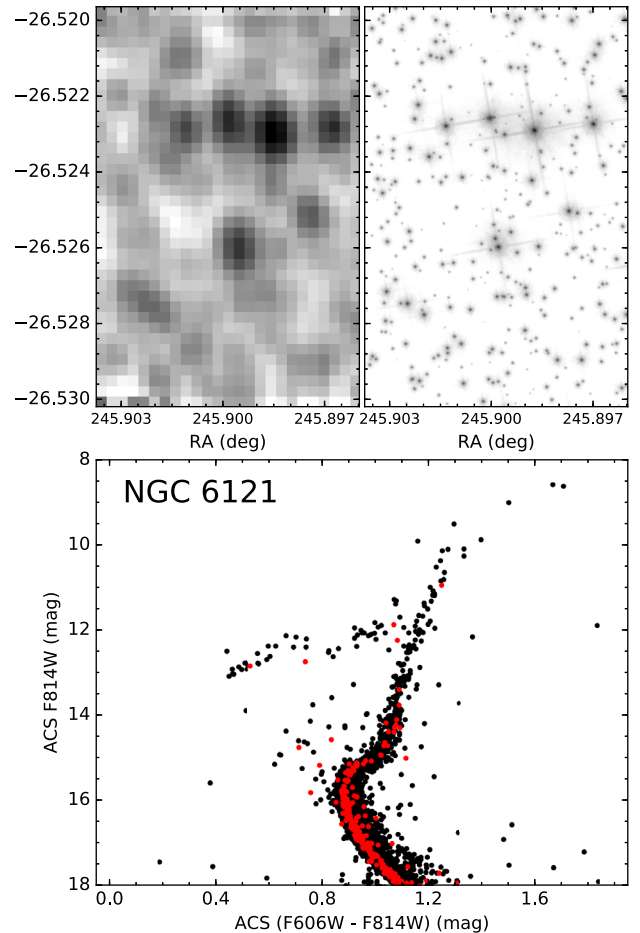


**Figure 13.** Comparison of the NGC 6121 WiFeS data cube with ACS imaging. Top left: WiFeS I7000 data cube collapsed along the wavelength direction. Top right: *HST*/ACS Wide Field Camera F814W image (GO-10775) of the same field of view as the WiFeS data cube. Bottom: ACS Globular Cluster Treasury Survey (Anderson et al. 2008) ( $F606W - F814W$ ) colour–magnitude diagram. Black points are all stars in the ACS catalogue, while red points are stars in the field of view of the WiFeS data cube. Our NGC 6121 data cube poorly samples the GC’s colour–magnitude diagram with only a handful of red giant branch and horizontal branch stars in the field of view. The brightest star in the field of view is an  $F814W=11$  red giant star, while faintest stars in the data cube that are not blends are subgiant branch stars with  $F814W\sim 15$ . We note that NGC 6121 is the closest GC in our sample and has the fourth lowest luminosity calculated enclosed by the field of view.

Multi-Pop). PC acknowledges the support provided by FONDECYT postdoctoral research grant no. 3160375 and by the Swinburne Chancellor Research Scholarship and the AAO PhD Topup Scholarship during the 2015 observing runs. SB acknowledges the support of the AAO PhD Topup Scholarship. This work made use of NUMPY (van der Walt, Colbert & Varoquaux 2011), SCIPY (Jones et al. 2001) and MATPLOTLIB (Hunter 2007) as well as ASTROPY, a community-developed core PYTHON package for astronomy (Astropy Collaboration et al. 2013). Additionally, this work made use of TOPCAT (Taylor 2005) and ALADIN (Bonnarel et al. 2000). This work was partially performed on the swinSTAR supercomputer at Swinburne University of Technology. This publication makes use of data products from the Two Micron All Sky Survey, which is a joint project of the University of Massachusetts and the Infrared Processing and

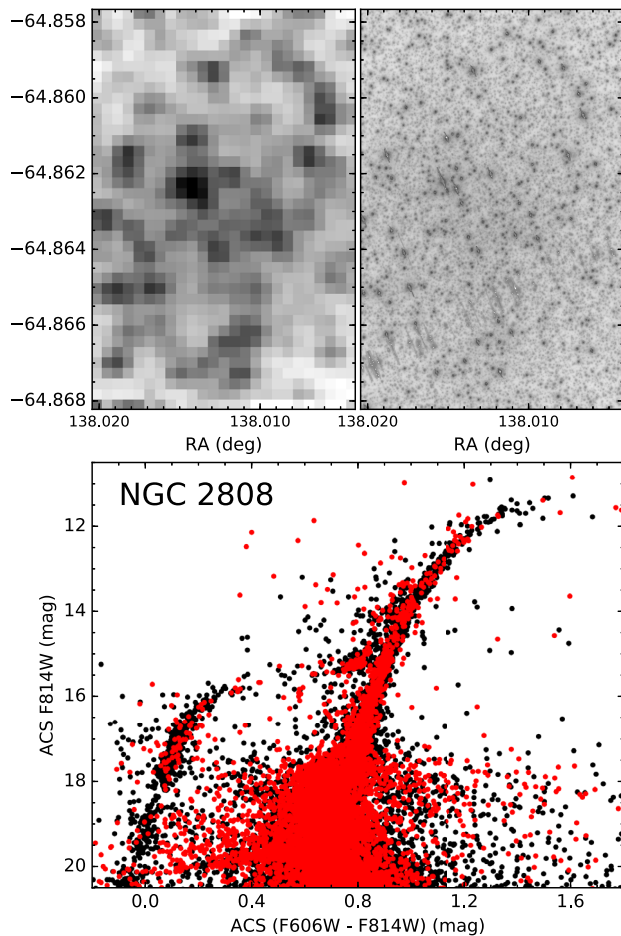


**Figure 14.** Comparison of the NGC 2808 WiFeS data cube with ACS imaging. Top left: WiFeS 17000 data cube collapsed along the wavelength direction. Top right: *HST*/ACS Wide Field Camera *F814W* image (GO-10775) of the same field of view as the WiFeS data cube. Bottom: ACS Globular Cluster Treasury Survey (Anderson et al. 2008) (*F606W* – *F814W*) colour–magnitude diagram. Black points are all stars in the ACS catalogue, while red points are stars in the field of view of the WiFeS data cube. The *HST* colour–magnitude diagram is well sampled by our observations. Our spatial coverage of NGC 2808 is typical of our sample although it is one of the more massive GCs in our sample.

Analysis Center/California Institute of Technology, funded by the National Aeronautics and Space Administration and the National Science Foundation. This research made use of Montage, funded by the National Aeronautics and Space Administration’s Earth Science Technology Office, Computational Technologies Project, under Cooperative Agreement Number NCC5-626 between NASA and the California Institute of Technology. The code is maintained by the NASA/IPAC Infrared Science Archive. This research has made use of the NASA/IPAC Extragalactic Database (NED), which is operated by the Jet Propulsion Laboratory, California Institute of Technology, under contract with the National Aeronautics and Space Administration. This research is based on observations made with the NASA/ESA *Hubble Space Telescope*, and obtained from the Hubble Legacy Archive, which is a collaboration between the Space Telescope Science Institute (STScI/NASA), the Space Telescope European Coordinating Facility (ST-ECF/ESA) and the Canadian Astronomy Data Centre (CAD/C/NRC/CSA).

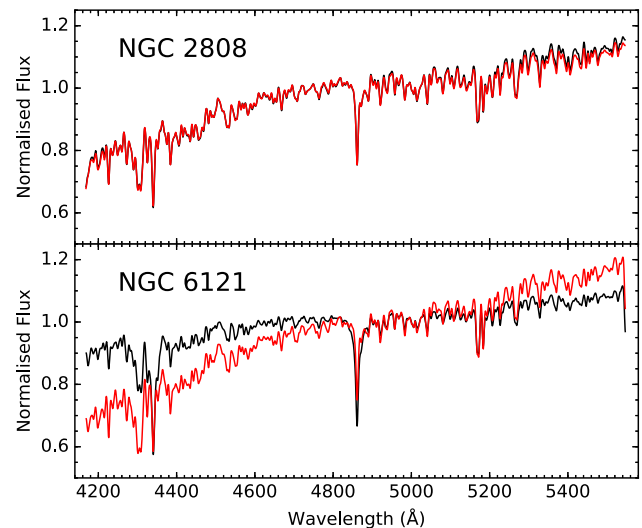


**Figure 15.** Effects of stochastic fluctuations in the number of stars within the field of view on the integrated spectra. In both panels, the spectrum extracted from the left-hand side of the B7000 cube is shown in black and the spectrum from the right in red. For the purposes of clarity, the spectra have been shifted to the rest frame, smoothed by a 5 Å FWHM Gaussian and normalized such that the mean flux at 5000 Å is unity. In the case of NGC 6121, where the observed light is dominated by a handful of red giant branch and horizontal branch stars, there are large differences in the shape of the continuum and the strengths of spectral features such as  $H\gamma$  and  $H\beta$  in the spectra from the two halves of the data cube. In the more typical case of NGC 2808, there are only minor but significant differences between the two halves.

## REFERENCES

- Anderson J. et al., 2008, *AJ*, 135, 2055  
 Andreuzzi G., Testa V., Marconi G., Alcaino G., Alvarado F., Buonoanno R., 2004, *A&A*, 425, 509  
 Armandroff T. E., Zinn R., 1988, *AJ*, 96, 92  
 Astropy Collaboration et al., 2013, *A&A*, 558, A33  
 Barbuy B., Zoccali M., Ortolani S., Hill V., Minniti D., Bica E., Renzini A., Gómez A., 2009, *A&A*, 507, 405  
 Bastian N., Lardo C., 2015, *MNRAS*, 453, 357  
 Bastian N., Silva-Villa E., 2013, *MNRAS*, 431, L122  
 Bastian N., Strader J., 2014, *MNRAS*, 443, 3594  
 Bastian N., Cabrera-Ziri I., Salaris M., 2015, *MNRAS*, 449, 3333  
 Baumgardt H., 2017, *MNRAS*, 464, 2174  
 Beasley M. A., Hoyle F., Sharples R. M., 2002, *MNRAS*, 336, 168  
 Beccari G., Dalessandro E., Lanzoni B., Ferraro F. R., Bellazzini M., Sollima A., 2015, *ApJ*, 814, 144  
 Bellazzini M., Ferraro F. R., Ibata R., 2003, *AJ*, 125, 188  
 Bica E., Alloin D., 1986, *A&A*, 162, 21  
 Bonnarel F. et al., 2000, *A&AS*, 143, 33  
 Brodie J. P., Hanes D. A., 1986, *ApJ*, 300, 258  
 Brodie J. P., Huchra J. P., 1991, *ApJ*, 379, 157  
 Brodie J. P. et al., 2014, *ApJ*, 796, 52  
 Bruzual G., Charlot S., 2003, *MNRAS*, 344, 1000  
 Burstein D., Faber S. M., Gaskell C. M., Krumm N., 1984, *ApJ*, 287, 586  
 Carretta E., Bragaglia A., Gratton R., D’Orazi V., Lucatello S., 2009, *A&A*, 508, 695  
 Carretta E. et al., 2010, *A&A*, 520, A95  
 Cenarro A. J., Cervantes J. L., Beasley M. A., Marín-Franch A., Vazdekis A., 2008, *ApJ*, 689, L29  
 Childress M., Vogt F., Nielsen J., Sharp R., 2014a, *Astrophysics Source Code Library*, record ascl:1402.034

- Childress M. J., Vogt F. P. A., Nielsen J., Sharp R. G., 2014b, *Ap&SS*, 349, 617
- Chung C., Yoon S.-J., Lee S.-Y., Lee Y.-W., 2016, *ApJ*, 818, 201
- Cohen J. G., Blakeslee J. P., Ryzhov A., 1998, *ApJ*, 496, 808
- Cole A. A., Smecker-Hane T. A., Tolstoy E., Bosler T. L., Gallagher J. S., 2004, *MNRAS*, 347, 367
- Colucci J. E., Bernstein R. A., Cameron S., McWilliam A., Cohen J. G., 2009, *ApJ*, 704, 385
- Colucci J. E., Bernstein R. A., Cameron S. A., McWilliam A., 2011, *ApJ*, 735, 55
- Colucci J. E., Bernstein R. A., McWilliam A., 2017, *ApJ*, 834, 105
- Conroy C., van Dokkum P. G., 2012, *ApJ*, 760, 71
- Conroy C., van Dokkum P. G., 2016, *ApJ*, 827, 9
- Conroy C., Gunn J. E., White M., 2009, *ApJ*, 699, 486
- Conroy C., Graves G. J., van Dokkum P. G., 2014, *ApJ*, 780, 33
- Conroy C., van Dokkum P. G., Choi J., 2015, *Nature*, 527, 488
- Covino S., Galletti S., Pasinetti L. E., 1995, *A&A*, 303, 79
- D'Ercole A., D'Antona F., Ventura P., Vesperini E., McMillan S. L. W., 2010, *MNRAS*, 407, 854
- Da Costa G. S., Hatzidimitriou D., 1998, *AJ*, 115, 1934
- Dalessandro E., Lapenna E., Mucciarelli A., Origlia L., Ferraro F. R., Lanzoni B., 2016, *ApJ*, 829, 77
- Davies B., Bastian N., Gieles M., Seth A. C., Mengel S., Konstantopoulos I. S., 2011, *MNRAS*, 411, 1386
- Davies B., Kudritzki R.-P., Gazak Z., Plez B., Bergemann M., Evans C., Patrick L., 2015, *ApJ*, 806, 21
- De Angeli F., Piotto G., Cassisi S., Busso G., Recio-Blanco A., Salaris M., Aparicio A., Rosenberg A., 2005, *AJ*, 130, 116
- de Boer T. J. L., Fraser M., 2016, *A&A*, 590, A35
- de Boer T. J. L. et al., 2012, *A&A*, 544, A73
- De Marchi G., Paresce F., Pulone L., 2007, *ApJ*, 656, L65
- de Mink S. E., Pols O. R., Langer N., Izzard R. G., 2009, *A&A*, 507, L1
- Decressin T., Meynet G., Charbonnel C., Prantzos N., Ekström S., 2007, *A&A*, 464, 1029
- Denissenkov P. A., Hartwick F. D. A., 2014, *MNRAS*, 437, L21
- Dopita M., Hart J., McGregor P., Oates P., Bloxham G., Jones D., 2007, *Ap&SS*, 310, 255
- Dopita M. et al., 2010, *Ap&SS*, 327, 245
- Dotter A. et al., 2010, *ApJ*, 708, 698
- Dotter A., Sarajedini A., Anderson J., 2011, *ApJ*, 738, 74
- Ferrelas I., La Barbera F., de la Rosa I. G., Vazdekis A., de Carvalho R. R., Falcón-Barroso J., Ricciardelli E., 2013, *MNRAS*, 429, L15
- Filippenko A. V., 1982, *PASP*, 94, 715
- Fischer P., Welch D. L., Mateo M., 1992, *AJ*, 104, 1086
- Forbes D. A., Kroupa P., 2011, *PASA*, 28, 77
- Forbes D. A. et al., 2017, *AJ*, 153, 114
- Foster C., Proctor R. N., Forbes D. A., Spolaor M., Hopkins P. F., Brodie J. P., 2009, *MNRAS*, 400, 2135
- Foster C., Forbes D. A., Proctor R. N., Strader J., Brodie J. P., Spitler L. R., 2010, *AJ*, 139, 1566
- Foster C. et al., 2011, *MNRAS*, 415, 3393
- Gallazzi A., Charlot S., Brinchmann J., White S. D. M., 2006, *MNRAS*, 370, 1106
- Geisler D., Bica E., Dottori H., Claria J. J., Piatti A. E., Santos J. F. C., Jr, 1997, *AJ*, 114, 1920
- Gieles M., Zocchi A., 2015, *MNRAS*, 454, 576
- Gilmore G. et al., 2012, *The Messenger*, 147, 25
- Glatt K. et al., 2008a, *AJ*, 135, 1106
- Glatt K. et al., 2008b, *AJ*, 136, 1703
- Glatt K. et al., 2009, *AJ*, 138, 1403
- Glazebrook K., Bland-Hawthorn J., 2001, *PASP*, 113, 197
- Goudfrooij P., Gilmore D., Kissler-Patig M., Maraston C., 2006, *MNRAS*, 369, 697
- Goudfrooij P., Puzia T. H., Kozhurina-Platais V., Chandar R., 2009, *AJ*, 137, 4988
- Goudfrooij P., Puzia T. H., Kozhurina-Platais V., Chandar R., 2011, *ApJ*, 737, 3
- Goudfrooij P. et al., 2014, *ApJ*, 797, 35
- Gratton R. G., Carretta E., Bragaglia A., 2012, *A&AR*, 20, 50
- Graves G. J., Schiavon R. P., 2008, *ApJS*, 177, 446
- Grocholski A. J., Cole A. A., Sarajedini A., Geisler D., Smith V. V., 2006, *AJ*, 132, 1630
- Hanes D. A., 1977, *MNRAS*, 180, 309
- Harris W. E., 1996, *AJ*, 112, 1487
- Harris J., Zaritsky D., 2009, *AJ*, 138, 1243
- Hilker M., Richtler T., 2000, *A&A*, 362, 895
- Hill V., 1999, *A&A*, 345, 430
- Hunter J. D., 2007, *Comput. Sci. Eng.*, 9, 90
- Husser T.-O. et al., 2016, *A&A*, 588, A148
- Ibata R. A., Wyse R. F. G., Gilmore G., Irwin M. J., Suntzeff N. B., 1997, *AJ*, 113, 634
- Johnson C. I., Pilachowski C. A., 2010, *ApJ*, 722, 1373
- Johnson J. A., Ivans I. I., Stetson P. B., 2006, *ApJ*, 640, 801
- Jones E. et al., 2001, *SciPy: Open source scientific tools for Python*, available at <http://www.scipy.org/>
- Kamann S., Wisotzki L., Roth M. M., 2013, *A&A*, 549, A71
- Kerber L. O., Santiago B. X., Brocato E., 2007, *A&A*, 462, 139
- King I. R., 1966, *AJ*, 71, 64
- Kobulnicky H. A. et al., 2005, *AJ*, 129, 239
- Koleva M., Prugniel P., Ocvirk P., Le Borgne D., Soubiran C., 2008, *MNRAS*, 385, 1998
- Kruijssen J. M. D., 2015, *MNRAS*, 454, 1658
- Lagioia E. P. et al., 2014, *ApJ*, 782, 50
- Lardo C., Bellazzini M., Pancino E., Carretta E., Bragaglia A., Dalessandro E., 2011, *A&A*, 525, A114
- Larsen S. S., Brodie J. P., Strader J., 2012, *A&A*, 546, A53
- Larsen S. S., Baumgardt H., Bastian N., Brodie J. P., Grundahl F., Strader J., 2015, *ApJ*, 804, 71
- Larsen S. S., Brodie J. P., Strader J., 2017, preprint ([arXiv:1702.07353](https://arxiv.org/abs/1702.07353))
- Law D. R., Majewski S. R., 2010, *ApJ*, 718, 1128
- Lebzelter T., Wood P. R., 2011, *A&A*, 529, A137
- Lee K. H., Lee H. M., Fahlman G. G., Lee M. G., 2003, *AJ*, 126, 815
- Mackey A. D., Gilmore G. F., 2003, *MNRAS*, 338, 85
- McLaughlin D. E., van der Marel R. P., 2005, *ApJS*, 161, 304
- APOGEE Team APOGEE-2 TeamMajewski S. R., 2016, *Astron. Nachr.*, 337, 863
- Marín-Franch A. et al., 2009, *ApJ*, 694, 1498
- Meissner F., Weiss A., 2006, *A&A*, 456, 1085
- Mészáros S. et al., 2015, *AJ*, 149, 153
- Mighell K. J., Sarajedini A., French R. S., 1998, *AJ*, 116, 2395
- Milone A. P. et al., 2014, *ApJ*, 785, 21
- Misgeld I., Mieske S., Hilker M., Richtler T., Georgiev I. Y., Schuberth Y., 2011, *A&A*, 531, A4
- Mucciarelli A., Ferraro F. R., Origlia L., Fusi Pecci F., 2007, *AJ*, 133, 2053
- Mucciarelli A., Carretta E., Origlia L., Ferraro F. R., 2008, *AJ*, 136, 375
- Mucciarelli A., Origlia L., Ferraro F. R., 2010, *ApJ*, 717, 277
- Mucciarelli A. et al., 2011, *MNRAS*, 413, 837
- Mucciarelli A., Origlia L., Ferraro F. R., Bellazzini M., Lanzoni B., 2012, *ApJ*, 746, L19
- Niederhofer F., Hilker M., Bastian N., Silva-Villa E., 2015, *A&A*, 575, A62
- Olsen K. A. G., Hodge P. W., Mateo M., Olszewski E. W., Schommer R. A., Suntzeff N. B., Walker A. R., 1998, *MNRAS*, 300, 665
- Olszewski E. W., Schommer R. A., Suntzeff N. B., Harris H. C., 1991, *AJ*, 101, 515
- Origlia L., Lena S., Diolaiti E., Ferraro F. R., Valenti E., Fabbri S., Beccari G., 2008, *ApJ*, 687, L79
- Pastorello N., Sarzi M., Cappellari M., Emsellem E., Mamon G. A., Bacon R., Davies R. L., de Zeeuw P. T., 2013, *MNRAS*, 430, 1219
- Pastorello N., Forbes D. A., Foster C., Brodie J. P., Usher C., Romanowsky A. J., Strader J., Arnold J. A., 2014, *MNRAS*, 442, 1003
- Pastorello N. et al., 2015, *MNRAS*, 451, 2625
- Patrick L. R., Evans C. J., Davies B., Kudritzki R.-P., Hénault-Brunet V., Bastian N., Lapenna E., Bergemann M., 2016, *MNRAS*, 458, 3968
- Paust N. E. Q. et al., 2010, *AJ*, 139, 476
- Pfeffer J., Griffen B. F., Baumgardt H., Hilker M., 2014, *MNRAS*, 444, 3670

- Piatti A. E., Geisler D., 2013, *AJ*, 145, 17
- Piotto G. et al., 2002, *A&A*, 391, 945
- Piotto G. et al., 2015, *AJ*, 149, 91
- Pipino A., Danziger I. J., 2011, *A&A*, 530, A22
- Puzia T. H., Saglia R. P., Kissler-Patig M., Maraston C., Greggio L., Renzini A., Ortolani S., 2002, *A&A*, 395, 45
- Puzia T. H., Kissler-Patig M., Thomas D., Maraston C., Saglia R. P., Bender R., Goudfrooij P., Hempel M., 2005, *A&A*, 439, 997
- Rood R. T. et al., 1999, *ApJ*, 523, 752
- Roth M. M., Becker T., Kelz A., Schmoll J., 2004, *ApJ*, 603, 531
- Sakari C. M., Shetrone M., Venn K., McWilliam A., Dotter A., 2013, *MNRAS*, 434, 358
- Sánchez-Blázquez P. et al., 2006, *MNRAS*, 371, 703
- Sarajedini A. et al., 2007, *AJ*, 133, 1658
- Schiavon R. P., 2007, *ApJS*, 171, 146
- Schiavon R. P., Barbuy B., Rossi S. C. F., Milone A., 1997, *ApJ*, 479, 902
- Schiavon R. P., Barbuy B., Bruzual A. G., 2000, *ApJ*, 532, 453
- Schiavon R. P., Rose J. A., Courteau S., MacArthur L. A., 2004, *ApJ*, 608, L33
- Schiavon R. P., Rose J. A., Courteau S., MacArthur L. A., 2005, *ApJS*, 160, 163
- Schuberth Y., Richtler T., Hilker M., Dirsch B., Bassino L. P., Romanowsky A. J., Infante L., 2010, *A&A*, 513, A52
- Searle L., Zinn R., 1978, *ApJ*, 225, 357
- Shapley H., 1918, *PASP*, 30, 42
- Sinnott B., Hou A., Anderson R., Harris W. E., Woodley K. A., 2010, *AJ*, 140, 2101
- Sirianni M., Nota A., De Marchi G., Leitherer C., Clampin M., 2002, *ApJ*, 579, 275
- Skrutskie M. F. et al., 2006, *AJ*, 131, 1163
- Smith R. J., Alton P., Lucey J. R., Conroy C., Carter D., 2015, *MNRAS*, 454, L71
- Strader J., Brodie J. P., 2004, *AJ*, 128, 1671
- Strader J., Caldwell N., Seth A. C., 2011a, *AJ*, 142, 8
- Strader J. et al., 2011b, *ApJS*, 197, 33
- Taylor M. B., 2005, in Shopbell P., Britton M., Ebert R., eds, *ASP Conf. Ser. Vol. 347, Astronomical Data Analysis Software and Systems XIV*. Astron. Soc. Pac., San Francisco, p. 29
- Usher C. et al., 2012, *MNRAS*, 426, 1475
- Usher C. et al., 2015, *MNRAS*, 446, 369
- Van der Swaelmen M., Hill V., Primas F., Cole A. A., 2013, *A&A*, 560, A44
- van der Walt S., Colbert S. C., Varoquaux G., 2011, *Comput. Sci. Eng.*, 13, 22
- van Dokkum P. G., 2001, *PASP*, 113, 1420
- van Dokkum P. G., Conroy C., 2014, *ApJ*, 797, 56
- VandenBerg D. A., Brogaard K., Leaman R., Casagrande L., 2013, *ApJ*, 775, 134
- Villanova S. et al., 2007, *ApJ*, 663, 296
- Willman B., Strader J., 2012, *AJ*, 144, 76
- Woodley K. A., Gómez M., Harris W. E., Geisler D., Harris G. L. H., 2010, *AJ*, 139, 1871
- Worthey G., 1994, *ApJS*, 95, 107
- Worthey G., Faber S. M., Gonzalez J. J., Burstein D., 1994, *ApJS*, 94, 687
- Zhu L. et al., 2014, *ApJ*, 792, 59
- Zinn R., West M. J., 1984, *ApJS*, 55, 45
- Zoccali M., Renzini A., Ortolani S., Bica E., Barbuy B., 2001, *AJ*, 121, 2638

## SUPPORTING INFORMATION

Supplementary data are available at [MNRAS](https://www.mnras.org) online.

### Table 2. Observing log.

Please note: Oxford University Press is not responsible for the content or functionality of any supporting materials supplied by the authors. Any queries (other than missing material) should be directed to the corresponding author for the article.

This paper has been typeset from a  $\text{\TeX}/\text{\LaTeX}$  file prepared by the author.